Studies of phase-change materials using ultrafast X-ray diffraction

Nilsson, Eric

2025

Studies of phase-change materials using ultrafast X-ray diffraction

ERIC NILSSON
DEPARTMENT OF PHYSICS | FACULTY OF ENGINEERING | LUND UNIVERSITY

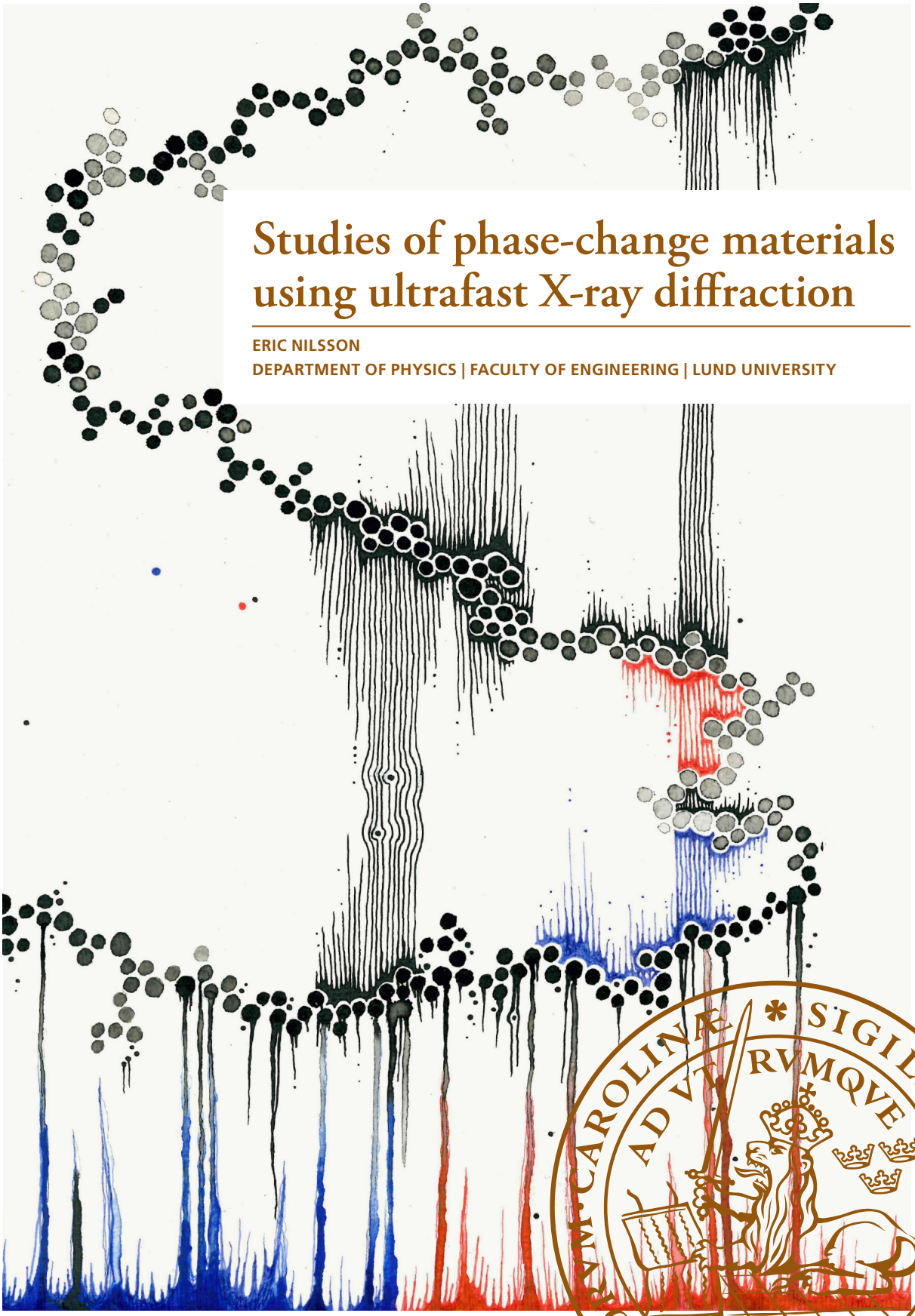

Printed by Media-Tryck, Lund 2025 NORDIC SWAN ECOLABEL 3041 0903

Faculty of Engineering
Department of Physics

LRAP: 619(2025)
ISBN 978-91-8104-747-9
ISSN 0281-2762

Studies of phase-change materials using ultrafast X-ray diffraction

Studies of phase-change materials using ultrafast X-ray diffraction

Eric Nilsson

LUND
UNIVERSITY

Akademisk avhandling som för avläggande av teknologie doktorsexamen vid tekniska fakulteten vid Lunds universitet kommer att offentligen försvaras den 28 november 2025, kl 13.15 i Rydbergssalen, på Fysiska institutionen, Professorsgatan 1, Lund.

Fakultetsopponent: Prof. Peter Balling
Aarhus University Aarhus, Danmark

Academic dissertation which, by due permission of the Faculty of Engineering at Lund University, will be publicly defended on November 28, 2025, at 13.15 in the Rydberg Lecture Hall, at the Department of Physics, Professorsgatan 1, Lund, for the degree of Doctor of Philosophy in Engineering.

Faculy opponent: Prof. Peter Balling
Aarhus University Aarhus, Denmark

Organization	Document name
LUND UNIVERSITY Department of Physics P.O. Box 118 SE–221 00 LUND Sweden	**DOCTORAL DISSERTATION** Date of disputation 2025-11-28 Sponsoring organization
Author(s) Eric Nilsson	

Title

Studies of phase-change materials using ultrafast X-ray diffraction

Abstract

This thesis is focused on the investigation of the ultrafast structural response of the phase change material (PCM) $Ge_2Sb_2Te_5$ following laser excitation. Phase change materials are a group of materials capable of rapid, non-volatile, switching between an amorphous and a crystalline phase. The two phases exhibit high optical and electrical contrast, meaning the optical reflectivity and the electrical conductivity differ significantly between the two phases. These properties make PCM suitable for data storage, and they have been widely used, mainly in DVD-RW discs. GST has been successfully used for Phase Change Random Access Memory (PCRAM), and the non-thermal excitation pathways have been the interest of numerous studies.

Conventionally, the phase change from the crystalline to the amorphous phase is driven by either optical or electric pulses on the order of 10 ns, where the material is melted and allowed to rapidly cool. If non-thermal pathways for amorphization exist, this could increase the write speed, up to 4 orders of magnitude.

This thesis presents ultrafast X-Ray Diffraction (XRD) studies investigating the ultrafast response of GST after femtosecond laser excitation, and compares the findings to previously suggested models, such as the suppression of the Peierls distortion, the umbrella flip model, and direct ultrafast amorphization. Furthermore, it is explained that the previous models do not satisfy the time-resolved behavior of the complete experimental findings, and a combination of these models is proposed as a more complete picture of the ultrafast dynamics

Key words

X-ray Diffraction, TRXRD, Ge2Sb2Te5, GST, Phase Change Material, PCM

Classification system and/or index terms (if any)

Supplementary bibliographical information	Language
	English
ISSN and key title 0281-2762 LRAP: 619(2025)	ISBN print:978-91-8104-747-9 pdf:978-91-8104-748-6
Recipient's notes	Number of pages 131 / Price
	Security classification

Studies of phase-change materials using ultrafast X-ray diffraction

by Eric Nilsson

LUND
UNIVERSITY

Studies of phase-change materials using
ultrafast X-ray diffraction

Department of Physics
Faculty of Engineering
Lund University

isbn: 978-91-8104-747-9 (print)
isbn: 978-91-8104-748-6 (pdf)
issn: 0281 – 2762

Printed in Sweden by Media-Tryck, Lund University, Lund 2025

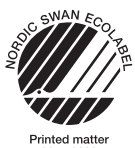

We live lives that are waveforms
constantly changing with time,
now positive, now negative.
Only at moments of great serenity
is it possible to find the pure,
the informationless state of signal zero.

-Thomas Pynchon

Abstract

This thesis is focused on the investigation of the ultrafast structural response of the phase change material (PCM) $Ge_2Sb_2Te_5$ following laser excitation. Phase change materials are a group of materials capable of rapid, non-volatile, switching between an amorphous and a crystalline phase. The two phases exhibit high optical and electrical contrast, meaning the optical reflectivity and the electrical conductivity differ significantly between the two phases. These properties make PCM suitable for data storage, and they have been widely used, mainly in DVD-RW discs. GST has been successfully used for Phase Change Random Access Memory (PCRAM), and the non-thermal excitation pathways have been the interest of numerous studies.

Conventionally, the phase change from the crystalline to the amorphous phase is driven by either optical or electric pulses on the order of 10 ns, where the material is melted and allowed to rapidly cool. If non-thermal pathways for amorphization exist, this could increase the write speed, up to 4 orders of magnitude.

This thesis presents ultrafast X-Ray Diffraction (XRD) studies investigating the ultrafast response of GST after femtosecond laser excitation, and compares the findings to previously suggested models, such as the suppression of the Peierls distortion, the umbrella flip model, and direct ultrafast amorphization. Furthermore, it is explained that the previous models do not satisfy the time-resolved behavior of the complete experimental findings, and a combination of these models is proposed as a more complete picture of the ultrafast dynamics

Populärvetenskaplig Sammanfattning

Datorer och datalagring har varit några av de viktigaste teknologiska framgångarna i samhället under det senaste seklet. Dessa teknologier har gjort det möjligt att kompakt lagra ofantliga mängder information och att dela denna information blixtsnabbt över hela världen. Vanligtvis lagras information i en dators minne av mycket små transistorer och kapacitorer, som bara ett tiotal nanometer stora. I en dator består dessa av kisel, som är en halvledare, vilket är ett mellanting mellan en isolator och en metall. Dessa par av transistorer och kapacitorer kallas bitar, och för att kunna använda bitarna för datalagring måste man kunna skilja på en 0:a och en 1:a, vilket i detta fallet görs genom att mäta hur många elektroner som finns i kapacitorerna. Nackdelen med dessa minnen är att de är flyktiga, vilket innebär att de bara kan bevara sin information när de försörjs med ström. Detta gör att metoden inte är praktisk för portabel datalagring, till exempel i CD- och DVD-skivor. I dessa används istället ett fasändringsmaterial som kallas GST.

Dessa fasändringsmaterial har flera stabila fasta faser och kan vara både kristallina och amorfa. En kristallin struktur innebär att atomerna är periodiskt ordnade i materialet, medan ett amorft material har en hög grad av oordning. Det vanligaste exemplet på ett amorft material är glas, som trots att det är ett fast material saknar en ordnad atomär struktur. Den amorfa fasen av GST kallas därför ofta för kalkogenglas, kalkogen för att GST innehåller tellur, som är en metall i gruppen kalkogener i det periodiska systemet. För att kunna använda dessa material för datalagring måste man kunna mäta en skillnad mellan faserna. Nyckeln är att GST uppvisar mycket stor skillnad i både optisk reflektivitet och elektrisk resistans mellan faserna. Man kan då med hjälp av antingen en kort laserpuls eller en elektrisk puls läsa av om materialet är en 0:a

eller en 1:a. Med hjälp av liknande pulser kan man även ändra fasen hos GST och på så sätt skriva data. Även detta görs med mycket korta pulser, omkring 100 ns långa. För att göra materialet kristallint, och på så sätt skriva en 1:a, värmer man det amorfa materialet över dess kristalliseringstemperatur, och låter det svalna långsamt tills det kristalliseras. För att amorfisera materialet, och skriva en 0:a, måste man först smälta det, och sedan låta det snabbt svalna så att det inte hinner kristalliseras.

För framtida minneslösningar, såsom Phase Change Random Access Memory (PCRAM), vill man kunna göra detta mycket snabbare, och helst undvika smältning. Detta har drivit omfattande forskning där man undersökt om det är möjligt att icke-termiskt amorfisera GST. Eftersom detta tar GST direkt från den kristallina fasen till den amorfa kan detta ske på några pikosekunder istället för på många nanosekunder, vilket innebär att det kan ske tiotusentals gånger snabbare.

I denna avhandling har detta undersökts med hjälp av ultrasnabb röntgendiffraktion. Denna metod untnytjar de periodiska strukturerna i kristallint GST och vågegenskaperna hos röntgenstrålning. Den röntgenstrålning som använts har en våglängd runt 0,1 nm, detta är nära avstånden mellan kristallplanen i GST som är runt 0,6 nm. Detta innebär att det kristallina materialet fungerar som en röntgenspegel för vissa specifika vinklar, enligt Braggs lag.

För att undersöka vad som sker direkt efter laserexcitation har ultrasnabba laserpulser, som är runt 100 fs långa, skickats in i materialet, och mycket kort därefter har lika korta röntgenpulser skickats in i materialet. Genom att studera hur den reflekterade röntgenstrålningen förändras kan man då utröna hur kristallstrukturen påverkats av laserpulsen.

Mätningarna har utförts på MAX IV anläggningen i Lund, vid strålröret FemtoMAX. Här accelereras elektroner i en linjäraccelerator till nära ljusets hastighet, och genom att oscillera elektronerna snabbt från sida till sida i en undulator skapas korta röntgenpulser. Tidigare modeller för dynamiken efter laserexcitation har undersökts, och nya modeller har lagts fram.

Popular Science Summary

Computers and data storage have been among the most important technological achievements in society over the past century. These technologies have allowed us to compactly store enormous amounts of information, and to share this information at lightning speed across the world. Typically, information in a computer's memory is stored using small transistors and capacitors, only a few tens of nanometers in size. In a computer, these components are made of silicon, which is a semiconductor — a material that is intermediate between an insulator and a metal. These pairs of transistors and capacitors are called bits, and in order to use the bits for data storage one must be able to distinguish between a 0 and a 1. In this case, the distinction is made by measuring how many electrons are present in the capacitors. The drawback of this type of memory is that it is volatile, meaning it can only retain its information when supplied with power. This makes the method impractical for portable data storage, such as CDs and DVDs. In these, instead, a phase-change material called GST is used.

These phase-change materials have several stable solid phases and can exist in both crystalline and amorphous forms. A crystalline structure means that the atoms are periodically arranged in the material, whereas an amorphous material has a high degree of disorder. The most common example of an amorphous material is glass, which, although solid, lacks any ordered atomic structure. The amorphous phase of GST is therefore often referred to as a chalcogenide glass — "chalcogenide" because GST contains tellurium, which is an element belonging to the chalcogen group in the periodic table.

To use these materials for data storage, one must be able to measure a difference between the phases. The key is that GST exhibits a large contrast in both optical reflectivity and electrical resistance between the crystalline and amorphous states. With the help of either a short laser pulse or an electrical

pulse, it is possible to read whether the material is in a “0” state or a “1” state. Using similar pulses, one can also change the phase of GST, thereby writing data. This is also done with short pulses, on the order of 100 nanoseconds. To make the material crystalline, and thus write a “1,” the amorphous material is heated above its crystallization temperature and annealed until it crystallizes. To amorphize the material, and thus write a “0,” the material must first be melted and then cooled rapidly so that it does not have time to crystallize.

For future memory technologies, such as Phase Change Random Access Memory (PCRAM), the goal is to achieve switching much faster, and ideally without the need for melting. This has driven extensive research into whether it is possible to amorphize GST through non-thermal pathways. Since this process would take GST directly from the crystalline phase to the amorphous phase, it could occur within a few picoseconds instead of many nanoseconds, meaning it could happen tens of thousands of times faster.

In this thesis, this has been investigated using ultrafast x-ray diffraction. This method takes advantage of the periodic structures in crystalline GST and the wave properties of X-rays. The X-ray radiation used has a wavelength of about 0.1 nm, which is close to the spacing between the crystal planes in GST, around 0.6 nm. This means that the crystalline material acts as an X-ray mirror for certain specific angles, in accordance with Bragg’s law [1].

To study what happens directly after laser excitation, ultrafast laser pulses, about 100 femtoseconds long, were fired at the material, and shortly afterward equally short X-ray pulses were directed at the material. From this, one can determine how the crystal structure has been affected by the laser pulse by studying how the reflected X-ray radiation changes.

The measurements were carried out at the MAX IV facility in Lund, at the FemtoMAX beamline. Here, electrons are accelerated in a linear accelerator to nearly the speed of light, and by rapidly oscillating the electrons side to side in an undulator, short X-ray pulses are generated. Previous models for the dynamics following laser excitation have been examined, and new models have been proposed.

Abbreviations

DCM	Double Crystal Monochromator
DRAM	Dynamic Random Access Memory
fs	femtosecond
GST	$Ge_2Sb_2Te_5$
MD	Molecular Dynamics
nm	nanometer
PCM	Phase Change Material
PCRAM	Phase Change Random Access Memory
ps	picosecond
RF	Radio-Frequency
TDS	Thermal Diffuse Scattering
TDDFT	Time-Dependent Density-Functional Theory Molecular Dynamics
TRXRD	Time-Resolved X-ray Diffraction
XRD	X-ray Diffraction

List of Publications

This thesis is based on the following publications, which are referred to by their Roman numerals.

I A cross-correlator-based timing tool for FemtoMAX
D. Kroon, E. Nilsson, B. Ahn, M. Bertelli, R. Calarco, I. Clementsson, S. De Simone, J. C. Ekström, A. Jurgilaitis, M. Longo, V. T. Phama and J. Larsson
Journal of Synchrotron Radiation **32** (2025)

II Laser induced coherent atomic motion in GST
E. Nilsson, I. Clementsson, B. Ahn, C. Ekström, D. Kroon, A. Jurgilaitis, M. Bertelli, R. Calarco, S. De Simeone, M. Longo, and J. Larsson
Manuscript in preparation

III The transition between Thermal and Non-Thermal Melting in InSb
E. Nilsson, Å. U. J. Bengtsson, I. Clementsson, J. C. Ekström, A. Jurgilaitis, Van-Thai Pham, D. Kroon, and J. Larsson
Manuscript in preparation

IV Debye-Waller factors and electron-phonon coupling time at high temperatures in fcc $Ge_2Sb_2Te_5$
E. Nilsson, I. Clementsson, B. Ahn, C. Ekström, D. Kroon, A. Jurgilaitis, M. Bertelli, R. Calarco, S. De Simeone, M. Longo, and J Larsson
Manuscript in preparation

Contents

Papers

Chapter 1

Introduction

Since the invention of computers, there has been ongoing research into making memory devices smaller and faster. Conventional modern computer memories, such as DRAM and FLASH, consist of silicon transistors and capacitors on the nanometer scale [2–4]. These memories are compact and fast, but looking into the next generation of memory technology, they both have considerable downside. DRAM is a fast, but volatile technology, which means that it needs power supply to store the data, and the complex structure of the capacitors prove complicated when considering stacking layers to create 3D structures [5, 6]. FLASH overcomes the issues of volatility, but instead suffers in speed [7, 8]. A different type of memory, called Phase Change RAM (PCRAM) shows promise in overcoming these limitations. These are based on the Phase Change Material (PCM) $Ge_2Sb_2Te_5$ (GST), which has been extensively used in CD-RW, DVD-RW, and rewritable Blu-ray [9–12]. Here, the data is stored in the different solid phases, where the amorphous phase is 0 and the crystalline phase is 1, and the data reading utilizes the high contrast in either optical reflectivity or electric conductivity between the two phases [13–15]. The main limitation at the moment is the write speeds, as amorphization is at the moment done by thermally melting the material, and allowing it to rapidly cool down, which takes a few tens of nanoseconds [16, 17].

For the past two decades, significant research has therefore been invested in achieving faster amorphization times, mainly through the process of non-thermal amorphization, where GST is driven directly from crystalline to amorphous using ultrafast laser pulses [18]. If realized, this could reduce the amorphization times dramatically, from 10-100 ns, down to a few picoseconds.

The experimental research has mainly been performed using ultrafast pump-probe techniques, where GST is excited by intense, short, laser pulses, on the fs scale, and subsequently probed using either optical probes, electron diffraction, X-ray diffraction or X-ray absorption spectroscopy [19–22]. This thesis covers the use of ultrafast X-ray diffraction, where the X-ray pulse duration is on the same time-scale as the pump pulses.

Conventional X-ray diffraction has been the staple technique for experimental crystallography since the beginning of the previous century, when the wave-nature of X-rays was understood, and it was for the first time demonstrated that crystals scatter diffract X-ray radiation. Up until the end of the century, conventional X-ray tubes and rotating anode X-ray generators were used for diffraction, before the advent of synchrotrons [23, 24].

Synchrotrons, such as the MAX IV facility in Lund, are circular electron accelerators, where the electrons in the orbit are accelerated close to the speed of light, and by bending the electron path, X-rays are generated, since an accelerated charge produces electromagnetic radiation [25]. The MAX IV facility consists of a linear accelerator, where the electrons are accelerated up to an energy of 3 GeV, and then inserted into either the 528 m circumference, 3GeV storage ring, or the smaller 96 m 1.5 GeV storage ring [26]. Insertion devices called undulators are placed periodically around the rings. These are made of permanent magnets, with periodic alternating magnetic fields in the electron beam direction, causing the electrons to wiggle back and forth when traveling through the undulators, generating intense X-ray radiation [27]. Downstream of the undulators are experimental stations which use the X-ray radiation for a number of different research applications, including diffraction.

The experimental station, or beamline, which has been used for the work in this thesis is the FemtoMAX beamline. This is the only beamline not connected to the rings, and instead receives electron pulses directly from the linear accelerator. Before the experimental station, these pulses pass two 5 m long, tunable undulators, generating ultrashort X-ray pulses, around 100 fs long, with tuneable energies from 2 keV to 20 keV, with photon fluxes up to $1 \cdot 10^7$ photons per pulse [28].

Connected to the X-ray beamline, in a lab upstairs, is a laser beamline. This beamline consist of a Ti:Sapphire based CPA system, which can produce pulses with energies up to 10 mJ, durations of 50 fs, and wavelength around 800 nm. This beamline is also equipped with a tuneable OPA system, where the wavelength can be tuned between 300 nm and 2500 nm.

The laser beamline and the X-ray beamline are synchronized using RF-signals from the linear accelerator. When conducting pump-probe experiments, the laser and X-ray pulses are overlapped on the material samples in the experimental chamber, and the relative arrival time of the two pulses can be adjusted with sub-ps accuracy. For higher experimental time-resolution, the data is post-sorted, using an RF-based timing monitor for coarse, around 200 fs, accuracy, and a cross-correlator based timing monitor for fine, around 30 fs, accuracy [29].

Thesis outline

This thesis aims to understand the ultrafast transient dynamics of crystalline $Ge_2Sb_2Te_5$ after laser excitation. The thesis consists of 5 chapters, where the first chapter gives a theoretical outline of matter, mainly crystallography, for understanding material properties needed for analyzing XRD experiments. The second chapter provides the theoretical background of X-ray interaction with matter, and explains the formalism for X-ray scattering from crystals. The third chapter covers the mechanisms with which visible and near-IR light interacts with matter, and how the energy is transferred from light to matter. The fourth chapter explains the method of time-resolved X-ray diffraction, and goes into detail on how to achieve fine temporal resolution. The fifth and final chapter delves into the material response of crystalline GST after laser excitation, and outlines previously suggested models, and finally results and a future outlook.

Chapter 2

Matter

This chapter provides the theoretical background for crystallography. The first part introduces the formalism for defining a crystal structure, and introduces concepts such as the lattice vectors and defining crystal planes using Miller indices. The second part discusses the reciprocal lattice, which is essential for using the Laue formulation for X-ray scattering. Finally, a description of Peierls distortion, and an overview of phase change materials, such as $Ge_2Sb_2Te_5$ is laid out.

2.1 Crystallography

Crystallography is a useful technique for characterizing solid materials. X-ray diffraction is a common and very powerful method used to determine the crystal structure of solids[30, 31]. When X-rays interact with electrons bound by atoms, they are scattered. For crystals, where the atoms are arranged in a crystal lattice, the intensity of the scattering for a certain angle depends on the spacing between the crystal planes. Thus, X-ray diffraction can be used to obtain detailed measurements of a crystal's structure, and be used to determine which materials are present, the symmetries of the crystals and the orientation of the crystals.

2.1.1 Perfect Crystals

A crystal is a collection of atoms that are ordered in a periodic structure. The smallest element that uniquely describes the crystal is called the unit cell, which is a parallelepiped with side lengths a_1, a_2 and a_3. The lattice vectors of the crystal are defined as vectors with magnitudes equal to the lengths of the side lengths, with orientations along the respective side lengths. Using the same convention, these vectors are then $\mathbf{a}_1$, $\mathbf{a}_2$ and $\mathbf{a}_3$.

A crystal can then be constructed by translating copies of the unit cell an integer amount along the lattice vectors. Unit cell m will be placed at

$$\mathbf{R}_m = m_1\mathbf{a}_1 + m_2\mathbf{a}_2 + m_3\mathbf{a}_3 \tag{1}$$

where m_1, m_2 and m_3 are all integers. Each point $\mathbf{R}_m$ is called a *lattice point*. If the position of atom j in the untranslated unit cell is denoted as $\mathbf{r}_j$, we can find the position of any atom j in any unit cell m by

$$\mathbf{R}_{m,j} = m_1\mathbf{a}_1 + m_2\mathbf{a}_2 + m_3\mathbf{a}_3 + \mathbf{r}_j. \tag{2}$$

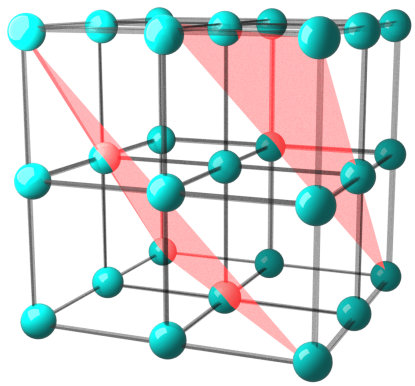

Figure 2.1: *Cubic crystal with the 111 planes indicated in red.*

It is very useful to describe different families of crystal planes using *Miller indices* [32]. A certain family of planes, hkl, is defined as the parallel and equidistant planes, where one plane cuts through $\frac{\mathbf{a}_1}{h}$, $\frac{\mathbf{a}_2}{k}$ and $\frac{\mathbf{a}_3}{l}$, and one plane passes through the origin. In Figure 2.1 is a collection of 8 unit cells where the 111 planes are indicated in red.

2.1.2 Reciprocal lattice

The *reciprocal lattice* is a useful concept when considering X-ray scattering from crystals [33, 34]. It is a set of points in what is usually called *reciprocal space*, and the points arise from a Fourier transform of the lattice points. Similar to the lattice vectors in real space, it is possible to construct reciprocal lattice vectors $\mathbf{b}_1$, $\mathbf{b}_2$ and $\mathbf{b}_3$, where the reciprocal lattice point hkl is located at

$$\mathbf{G}_{hkl} = h\mathbf{b}_1 + k\mathbf{b}_2 + l\mathbf{b}_3 \tag{3}$$

where h, k and l are integers. The reciprocal lattice vectors can be defined as

$$\mathbf{b}_1 = 2\pi\frac{\mathbf{a}_2 \times \mathbf{a}_3}{\mathbf{a}_1 \cdot \mathbf{a}_2 \times \mathbf{a}_3}, \quad \mathbf{b}_2 = 2\pi\frac{\mathbf{a}_3 \times \mathbf{a}_1}{\mathbf{a}_1 \cdot \mathbf{a}_2 \times \mathbf{a}_3} \quad \text{and} \quad \mathbf{b}_3 = 2\pi\frac{\mathbf{a}_1 \times \mathbf{a}_2}{\mathbf{a}_1 \cdot \mathbf{a}_2 \times \mathbf{a}_3} \tag{4}$$

where $\mathbf{a}_1$, $\mathbf{a}_2$ and $\mathbf{a}_3$ are the lattice vectors.

A vector $\mathbf{H}_{hkl} = h\mathbf{b}_1 + k\mathbf{b}_2 + l\mathbf{b}_3$, described by the reciprocal lattice vectors, is perpendicular to the Miller planes with indices hkl [35, 36].

2.1.3 Peierls distortion

We have thus far introduced perfect crystals with high orders of symmetry. This is not always the state in which we encounter materials, oftentimes they have distortions. These distortions can come from excitations, and, for some materials, the natural ground state at room temperature is distorted. The main type of distortion that is of interest for this work is the A7 distortion, which consist of a Peierls distortion and a rhombohedral distortion [37, 38]. Let us first consider the 1D Peierls distortion by looking at a 1D chain of atoms as seen in Figure 2.2 a).

When the spacing between the atoms is a for every atom, the periodicity of the Brillouin zone will be $\frac{\pi}{a}$, and the band structure will be a simple cosine dependence as shown in Figure 2.2 b) [39]. It is also possible to consider grouping the atoms two and two, the resulting Brillouin zone would then have a periodicity of $\frac{\pi}{2a}$ as is indicated by the dashed lines in Figure 2.2 b).

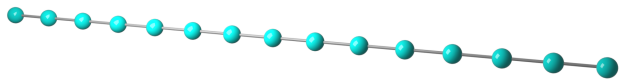

(a) Undistorted 1D chain of atoms.

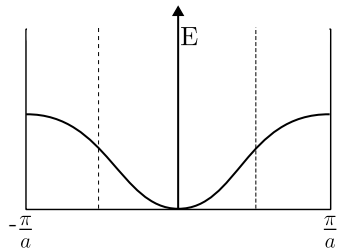

(b) Band structure for 1D chain of atoms.

Figure 2.2: *a) A 1D chain of atoms with one electron per atom b) The resulting band structure.*

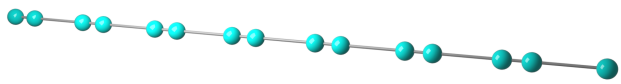

(a) 1D chain of atoms with a Peierls distortion.

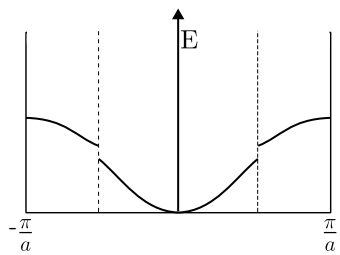

(b) Band structure of Peierls distorted 1D chain of atoms.

Figure 2.3: *a) A 1D chain of atoms with one electron per atom, where the spacing between atoms is not equal, but instead distorted with a 1D Peierls distortion b) The resulting band structure.*

If we now dimerize the chain by moving every other atom a distance Δa, we introduce what is called Peierls distortion, as is shown in Figure 2.3 a). This will result in a splitting of the energy band as seen in Figure 2.3 b). Since the bands will only be occupied for $-\frac{\pi}{2a} \leq k \leq \frac{\pi}{2a}$, the distortion lowers the energy for all occupied states, while increasing the energy for all unoccupied states, which, if the atomic chain is at low temperature, lowers the energy for the whole system. This means that any such system, where this electronic energy gain is greater than the mechanical energy losses from the strain, will strive to undergo a Peierls distortion.

An important material for this work is $Ge_2Sb_2Te_5$ which has one metastable crystalline, rock-salt phase, which exhibits A7 distortion with a Peierls distortion along the [111] direction, where the cation and anion ions are moved with respect to each other [40, 41].

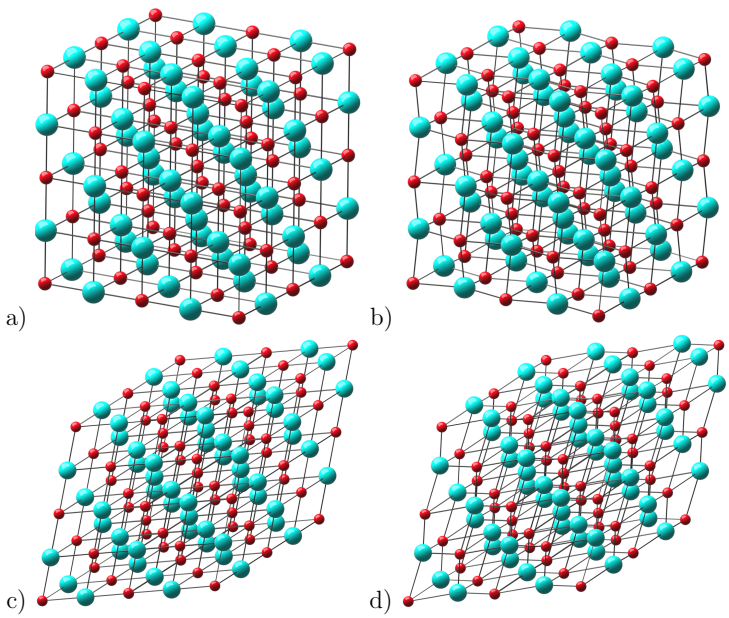

Figure 2.4: *a) Undistorted rock-salt structure, with Na as red atoms and Cl as blue atoms. b) The same structure which has undergone Peierls distortion along the [111] direction. c) The same structure with a rhombohedral distortion along the [111] direction. d) The same structure with the full A7 distortion, a combination of the distortion in b and c.*

The undistorted rock-salt structure can be seen in Figure 2.4 a), where the blue atoms are the sodium atoms and the red atoms the chlorine atoms. In Figure 2.4 b), the sodium lattice and the chlorine lattice have been displaced with respect to each other along the [111] direction. As can be seen in the Figure, this Peierls distortion makes the distance between the sodium planes and the chlorine planes, which are parallel to the [111] planes, alternate. Just like in the 1D case where the bonds alternate between long and short bonds, so will the plane spacing alternate between a long spacing and a short spacing. Furthermore, if we look at a single chlorine atom, it will have six neighboring sodium atoms, where, after the distortion, three of the bonds will be long and three of the bonds short. Thus, the magnitude of the Peierls distortion can be measured by measuring the length of the short and long bonds.

The other type of distortion which describes the A7 distortion is a rhombohedral distortion along the [111] direction as shown in 2.4 c), where the whole unit cell is stretched in the [111] direction and compressed in the plane perpendicular to the [111] direction. Finally, in Figure 2.4 d), we see the full A7 distortion, consisting of both a Peierls distortion, and a rhombohedral distortion along the [111] direction [40, 41].

2.2 Phase change materials

Many materials can exist in several different stable solid phases. Some of these materials can exist in an amorphous solid phase, even though there exists one, or more, thermodynamically stable phases. For some of these materials, it is possible to repeatedly, and with a high degree of control, switch the material between the amorphous phase and one of the crystalline phases. These materials are what we call phase change materials (PCMs) [42]. Many of the PCMs that are of interest for data storage belong to the group of materials called chalcogenides. This group contains both some of the first discovered PCM, containing tellurium, arsenide, silicon and germanium, and the most utilized PCM $Ge_2Sb_2Te_5$ (GST) [43]. What makes these materials useful for storing information, is that very large contrasts between the two phases, for different material properties can exist. As an example, GST exhibits a high optical contrast, which means a high difference in reflectivity between the amorphous and the metastable rock-salt phase. It also exhibits a large change in electrical conductivity between these two phases [44].

These contrasts are what makes the materials, and their phase changing

capabilities, useful for data storage [45]. For GST, the material is initialized to the crystalline phase, usually by laser annealing at a low temperature. Thus, the signal from the crystalline material is interpreted as "1". Then, to write data, the usual method is to heat the material above the melting point using a laser, and letting it rapidly cool down to the amorphous phase. In optical storage, such as DVD-R discs [46], the lower reflectivity of the amorphous phase is what makes it possible to distinguish it from the more reflective crystalline phase, by sending a probe laser on to the disk and measuring the reflected light [47].

Chapter summary

This chapter outlines the theoretical basis for crystallography, how the crystal structure is defined and how Peierls distortion affects the structure. It ends with a brief introduction of phase change materials and GST. The next chapter introduces how X-rays interact with matter, and theory about the scattering process which is used in the thesis.

Chapter 3

X-ray interaction with matter

X-ray diffraction is the most powerful technique used for probing the structure of crystalline materials, such as metals and semi-conductors. X-rays get scattered by electrons bound by the atoms in materials. Due to the wave-nature of X-rays, and the fact that the wave-length of X-rays are of about the same order as the interatomic distances in solids, the X-ray scattering is determined by the atomic plane spacing of the crystals. This causes different atomic structures to generate a unique scattering pattern, depending on the atoms present in the material, their arrangement in the unit cell, the spacing between the atomic planes, and several other measurable properties such as the temperature and strain in the material.

This chapter lays out the theoretical background for X-ray diffraction. The first part aims to explain how X-rays scatter from materials, by first showing how X-rays scatter from free electrons, and from there build up the general theory of X-ray diffraction. Following this, a few applied techniques such as powder diffraction and diffuse scattering are discussed.

3.1 X-ray scattering

When X-ray radiation interacts with matter, it mainly interacts with the electrons in the material. The X-ray photons can be either scattered by the

electrons, or deposit their energy to the electron, kicking the electron out of its bound state. In the following sections, the main focus will be on the scattering processes, since these are the main points of interest for this work.

3.1.1 X-ray scattering from a free electron

An electron is a charged particle, and will experience a force when in an electric field

$$\mathbf{F} = q\mathbf{E} \tag{1}$$

where q is the electron charge and E the electric field [48]. Since electromagnetic radiation has an oscillating electric field component

$$\mathbf{E}_0(r,t) = \mathrm{Re}\{E_0(r)\exp(j\omega t)\} \tag{2}$$

where E_0 is the amplitude of the electric field, and ω is the angular frequency, a free electron will experience an oscillating force, and in turn, an oscillating acceleration [49].

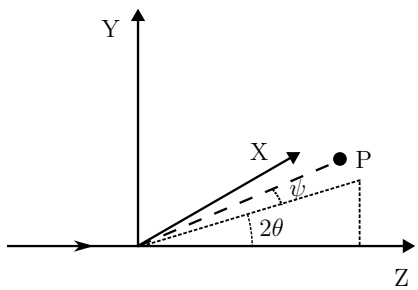

Figure 3.1: *Scattering of X-rays polarized in the x-direction traveling in the z-direction by an electron at the origin, as observed by an observer at point P.*

Consider a free electron at rest at the origin of a coordinate system. Let an X-ray beam travel along the z-axis with polarization along the x-axis, as shown in Figure 3.1. The X-rays will cause the electron to oscillate along the x-axis and, in turn, emit dipole radiation. The acceleration of the electron will be

$$\mathbf{a} = \frac{q\mathbf{E}_0}{m} \tag{3}$$

where m is the electron mass, and $\mathbf{E}_0$ is the incoming electric field.

The amplitude of the resulting electric field at an observer, P, will depend on the distance $|\mathbf{r}|$, where $\mathbf{r}$ is the vector from O to P, and the perceived acceleration $\mathbf{a}_\perp$, which is the component of the acceleration perpendicular to $\mathbf{a}$. The direction of the resulting electric field will be in the same direction as $\mathbf{a}_\perp$. In cgs units the electric field at point P is

$$\mathbf{E} = \frac{q\mathbf{a}\cos(\Psi)}{c^2|\mathbf{r}|} \tag{4}$$

where Ψ is the angle between $\mathbf{r}$ and the plane normal to the polarization direction and c is the speed of light. With the expression of the acceleration we arrive at

$$\mathbf{E} = \frac{e^2 E_0}{mc^2|\mathbf{r}|}\cos(\Psi)\cos(\omega t)\hat{\mathbf{n}}_\perp \tag{5}$$

where e is the elementary charge and $\hat{\mathbf{n}}_\perp$ is a unit vector in the direction of $\mathbf{a}_\perp$ [50].

3.1.2 X-ray scattering from atoms

The scattering from an atom is the scattering from all the individual electrons in the atom. We will mainly focus on resonant scattering, that is, scattering where the wavelength is the same before and after the scattering process. This is also called unmodified scattering.

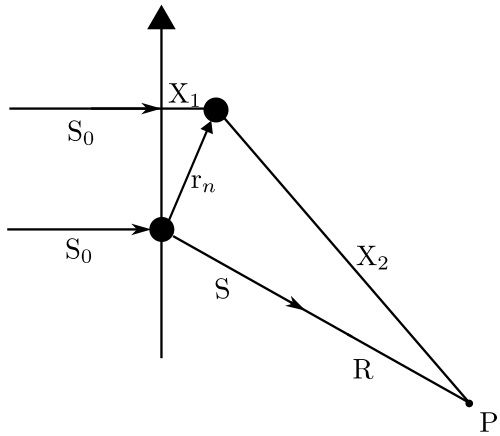

Figure 3.2: *Scattering at point P from two atoms separated by r_n*

Consider a plane wave S_0, interacting with atoms n at position r_n. Compared to an electron at the origin, the scattered light will have traveled a distance X_1+X_2-R longer, and thus acquired an extra phase $\frac{2\pi}{\lambda}(X_1 + X_2)$. If we assume that R$\gg$r$_n$, we can approximate this as $\frac{2\pi}{\lambda}(r_n \cdot S_0 + R - r_n \cdot S)$. If we now use the complex form of Equation 5, we can write the electric field from electron n at position P as

$$\mathbf{E}_n = \frac{e^2 E_0}{mc^2 \mathrm{R}} e^{\omega t - \frac{2\pi}{\lambda}\mathrm{R}} e^{\frac{2\pi}{\lambda}(\mathrm{S}-\mathrm{S}_0)r_n}. \tag{6}$$

The sum of the intensity from all electrons will then be

$$\mathbf{E} = \frac{e^2 E_0}{mc^2 \mathrm{R}} e^{\omega t - \frac{2\pi}{\lambda}\mathrm{R}} \sum_n e^{\frac{2\pi}{\lambda}(\mathrm{S}-\mathrm{S}_0)r_n}. \tag{7}$$

This expression would be accurate if the scattering from the electrons could be described as scattering from classical point particles, which is the assumption that has been made. This can be remedied by changing the sum in expression 7 to an integral

$$\mathbf{E} = \frac{e^2 E_0}{mc^2 \mathrm{R}} e^{\omega t - \frac{2\pi}{\lambda}\mathrm{R}} \int e^{\frac{2\pi}{\lambda}(\mathrm{S}-\mathrm{S}_0)r_n} \rho dV \tag{8}$$

where ρ is the charge density of all the electrons.

The integration part of equation 8 is called the scattering factor per electron, f_e. Assuming spherical symmetry of the charge density, this expression can be solved for the whole atom, by considering each electron separately, as

$$f = \sum_n \int 4\pi \boldsymbol{r}^2 \rho_n(\boldsymbol{r}) \frac{\sin k\boldsymbol{r}}{k\boldsymbol{r}} d\boldsymbol{r} \quad , \tag{9}$$

where $k = \frac{4\pi \sin(\theta)}{\lambda}$. The quantity f is known as the atomic scattering factor.

3.1.3 Bragg's law

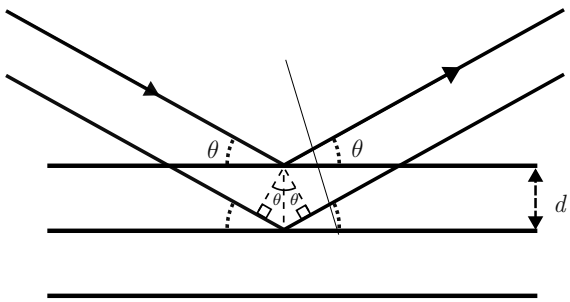

Figure 3.3: *Schematic of the scattering condition fulfilling Bragg's law with plane spacing d and incidence angle θ.*

When light is scattered from a set of parallel planes, the scattered light from each plane will interfere. Depending on the incoming wavelength, λ, the spacing between the planes, d, and the angle the incoming light makes with the surface, θ, the outgoing light will interfere either constructively or destructively. If these parameters are just right, the light from each consecutive plane will travel an integer number of wavelengths further than the light scattered from the first layer, and the scattered light from all layers will interfere constructively. As shown in Figure 3.3, the scattered light from each plane will have traveled a distance $2d\sin(\theta)$ longer than the scattered light from the previous plane. Since the scattered light from the different planes will be in phase if the difference in distance traveled is an integer

number of wavelengths, the condition that has to be fulfilled is

$$m\lambda = 2d\sin\theta \tag{10}$$

which is called Bragg's law [1]. For X-rays, the spacing between atomic planes in crystal is of the same order of magnitude as the wavelength. Thus, X-rays are a great tool for investigating the structure of crystals. The bright reflected spot that arises when X-ray light satisfies the Bragg condition is called a Bragg spot.

3.1.4 Laue formulation

Another, equivalent, way of determining the scattering from a crystal is using the *Laue* equations. Instead of using the real-space characteristics of the crystals, the reciprocal space formalism is used instead. Consider incoming X-rays with wave-vector $\mathbf{k}_{in} = \frac{1}{\lambda}\mathbf{s}_{in}$ and scattered X-rays with wave-vector $\mathbf{k}_{out} = \frac{1}{\lambda}\mathbf{s}_{out}$, where λ is the X-ray wavelength and $\mathbf{s}_{in}$ and $\mathbf{s}_{out}$ are the normalized directions of the incoming and scattered X-rays, respectively, we can then define the scattering vector $\Delta\mathbf{k} = \mathbf{k}_{out} - \mathbf{k}_{in}$.

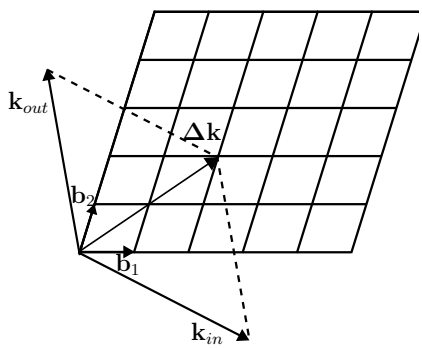

Figure 3.4: *Incoming and scattered X-rays fulfilling the Laue equations.*

The equations that need to be fulfilled for constructive interference of the scattered light are then

$$\begin{aligned} \Delta\mathbf{k} \cdot \mathbf{a}_1 &= h \\ \Delta\mathbf{k} \cdot \mathbf{a}_2 &= k \\ \Delta\mathbf{k} \cdot \mathbf{a}_3 &= l \end{aligned} \tag{11}$$

where $\mathbf{a}_1$, $\mathbf{a}_2$ and $\mathbf{a}_3$ are the lattice vectors. These equations can also be re-written as

$$\Delta\mathbf{k} = \mathbf{G}_{hkl} \tag{12}$$

which is shown in Figure 3.4 [51].

3.1.5 Ewald's sphere

Related to the Laue equations is another very useful concept, the Ewald's sphere. If we consider the incoming X-rays as a vector $\mathbf{k}_{in}$ which terminates at the origin, the Ewald's sphere is the sphere defined by all the points in reciprocal space that are a distance $|\mathbf{k}_{in}|$ away from the tail of $\mathbf{k}_{in}$, as shown in Figure 3.5 [33].

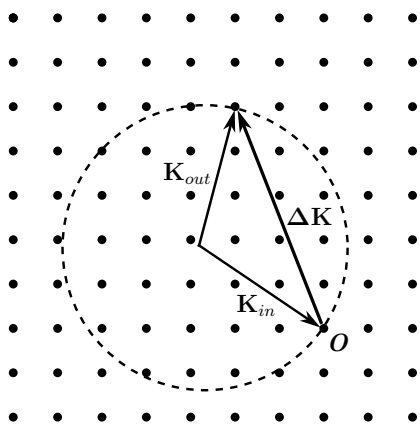

Figure 3.5: *The Ewald's sphere in 2 dimensions where the direction of the scattered X-rays are determined by which reciprocal lattice point the Ewald's sphere cuts through.*

The scattering condition is fulfilled if any reciprocal lattice points lay on the Ewald's sphere. If that is the case, the scattered X-rays will travel in the direction from the tail of $\mathbf{k}_{in}$ towards the specified reciprocal lattice point which resides on the Ewald's sphere [52].

3.1.6 Structure factor

We have so far, in this chapter, only considered the effects of the lattice, and not taken into account how the scattering is depends on how the atoms are arranged in each unit cell. It is useful to here use the same convention as in Chapter 2.1.1, and let $\mathbf{r}_j = x_j\mathbf{a}_1 + y_j\mathbf{a}_2 + z_j\mathbf{a}_3$, where x_j, y_j and z_j are allowed to also take fractional values. If we now consider the scattering in a direction which satisfies the Laue equations, $\Delta\mathbf{k} = \mathbf{S}_0 - \mathbf{S} = \mathbf{G}_{hkl}$, the scattering intensity will also depend on the location of the atoms within the unit cell, with the term

$$F_{hkl} = \sum_n f_n e^{2\pi i(h\mathbf{b}_1 + k\mathbf{b}_2 + l\mathbf{b}_3)\cdot(\mathbf{x}_n\mathbf{a}_1 + \mathbf{y}_n\mathbf{a}_2 + \mathbf{z}_n\mathbf{a}_3)} \tag{13}$$

where F_{hkl} is called the structure factor [53]. Since we chose a direction where the Laue equations are satisfied, this simplifies to

$$F_{hkl} = \sum_n f_n e^{2\pi i(h\mathbf{x}_n + k\mathbf{y}_n + l\mathbf{z}_n)}. \tag{14}$$

Two important crystal structures for this work is the rock-salt structure and the zinc-blende structure. The rock-salt structure, which is the structure for $Ge_2Sb_2Te_5$, can be determined from the location of four Na and four Cl atoms. Let us consider equation 14 for Cl and Na atoms at positions

$$\text{Cl} \begin{matrix} 0 & 0 & 0 \\ 0 & \frac{1}{2} & \frac{1}{2} \\ \frac{1}{2} & 0 & \frac{1}{2} \\ \frac{1}{2} & \frac{1}{2} & 0 \end{matrix} \qquad \text{Na} \begin{matrix} \frac{1}{2} & \frac{1}{2} & \frac{1}{2} \\ 0 & 0 & \frac{1}{2} \\ 0 & \frac{1}{2} & 0 \\ \frac{1}{2} & 0 & 0 \end{matrix} .$$

We then get the expression for the structure factor

$$F_{hkl} = f_{Cl}\left[1 + e^{\pi i(k+l)} + e^{\pi i(h+l)} + e^{\pi i(h+k)}\right] + f_{Na}\left[+e^{\pi i(h+k+l)} + e^{\pi il} + e^{\pi ik} + e^{\pi ih}\right] \tag{15}$$

which gives $F_{hkl} = 0$ if h, k and l are mixed both even and odd, and $F_{hkl} = 4\left[f_{Cl} + f_{Na}e^{\pi i(h+k+l)}\right]$ if h, k and l are all both even or odd [54]. Further simplification for the unmixed case gives the structure factor

$$\begin{aligned} hkl \quad &\text{even} \quad F_{hkl} = 4(f_{Cl} + f_{Na}), \\ hkl \quad &\text{odd} \quad F_{hkl} = 4(f_{Cl} - f_{Na}). \end{aligned} \tag{16}$$

The fact that the structure factor is zero when h, k and l are mixed is true for every face centered cubic(fcc) crystal structure. The zinc-blende structure is also an fcc structure, and the structure factor can be determined from Zn and S atoms at positions

$$\text{Zn} \quad \begin{matrix} 0 & 0 & 0 \\ \frac{1}{2} & \frac{1}{2} & 0 \\ \frac{1}{2} & 0 & \frac{1}{2} \\ 0 & \frac{1}{2} & \frac{1}{2} \end{matrix} \qquad \text{S} \quad \begin{matrix} \frac{1}{4} & \frac{1}{4} & \frac{1}{4} \\ \frac{3}{4} & \frac{3}{4} & \frac{1}{4} \\ \frac{3}{4} & \frac{1}{4} & \frac{3}{4} \\ \frac{1}{4} & \frac{3}{4} & \frac{3}{4} \end{matrix} \quad .$$

For the mixed case we again have that $F_{hkl} = 0$, and for the unmixed case we have $F_{hkl} = 4\left[f_{Zn} + f_S e^{\frac{\pi i}{2}(h+k+l)}\right]$, which gives the cases

$$\begin{aligned} &h+k+l = 4n && F_{hkl}^2 = 16(f_{Zn} + f_S)^2, \\ &h+k+l = 2(2n+1) && F_{hkl}^2 = 16(f_{Zn} - f_S)^2, \\ &hkl \text{ all odd} && F_{hkl}^2 = 16(f_{Zn}^2 + f_S^2) \end{aligned} \tag{17}$$

when h, k and l are unmixed.

3.2 Powder diffraction

Some of the samples in this work were polycrystalline samples, consisting of many small, randomly oriented, grains of crystalline material. The scattering that arises from these samples is very similar to the scattering from powder patterns, and differ quite dramatically from scattering pattern from single-crystalline materials. In this section the powder diffraction method will be discussed.

3.2.1 Cone of diffraction

To get X-ray diffraction, Bragg's law, or, equivalently, the Laue equations, has to be fulfilled. For a single crystal this results in at most one scattered point for each set of planes hkl which satisfy the Bragg condition. This is not the case if we consider the scattering from a powder consisting of many small, randomly oriented, crystallites. Instead, there will exist some crystallite

fulfilling the Bragg condition for every set of planes, hkl, in every direction, where $d_{hkl} \geq \frac{\lambda}{2}$, according to Bragg's law [55].

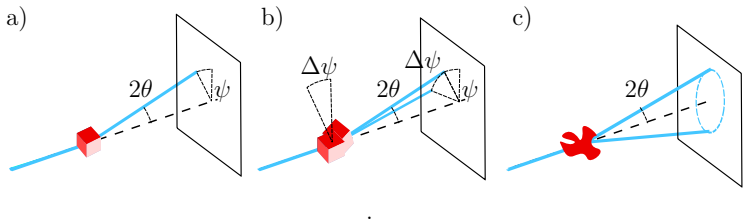

Figure 3.6: *Schematic showing the principles of powder diffraction. a) A single crystallite fulfilling the Bragg condition for a certain set of planes hkl, resulting in diffracting angle 2θ and azimuthal angle $\Delta\psi$ b) Two crystallites fulfilling the Bragg condition for the same set of planes hkl, where one is rotated an angle ψ with respect to the other crystallite, causing the azimuthal angle of the diffracted beam to be rotated by the same angle θ. c) A collection of a large amount of crystallites, all fulfilling the Bragg condition for the same set of planes hkl, with crystallites with every possible rotation $\Delta\psi$*

Considering a single crystallite, which satisfies the Bragg condition for some set of planes hkl. The diffracted signal from this crystallite will have scattering angle 2θ, and azimuthal angle ψ with respect to the incoming X-rays. Another crystallite with the same orientation, except rotated an angle $\Delta\psi$ around the incoming X-ray direction, will also satisfy the Bragg condition, but the scattered intensity will instead make angles $\theta, \psi + \Delta\psi$ with respect to the incoming X-ray direction, as shown in Figure 3.6. If there are enough crystallites, which is an assumption which is often made for powder diffraction, a crystallite will exist for every angle $0 \geq \Delta\psi \geq 2\pi$, which results in a cone of diffracted X-ray radiation. This will not only be true for one set of planes hkl, but for every set of planes which can fulfill the Bragg condition, resulting in a number of diffracted cones with half apex angles 2θ, as shown in figure 3.6 c).

On a detector which is normal to the incident beam this will show up as a set of concentric rings, but if the detector is tilted this will instead show up as conic sections.

3.2.2 Analyzing powder pattern

When looking at a powder diffraction signal, compared to the signal from a single-crystalline material, a lot of the information is lost. This is because, instead of looking at a full 3D image in reciprocal space, we instead look at a 1D signal, since the signal strength is dependent only on the scattering angle θ. However, a lot of information about the structure of the crystal can be retrieved, and powder diffraction is still a very powerful tool.

The most common way of recording powder diffraction data is by using a 1D detector, kept at a constant distance R from the sample, and rotating it with an angular velocity ω in a circular arc. What is recorded is then the intensity for each scattering angle θ. Since the magnitude of the scattering vector, Q, can be expressed in terms of θ as

$$Q = \frac{4\pi}{\lambda}\sin(\theta) \quad , \tag{18}$$

it is possible to express the intensity as function of Q, which only depends on the crystal itself, and not on the measurement variables.

For each angle θ, which satisfies the Bragg condition, a strong scattering peak will be recorded. The relative strength of each peak will be dependent on a number of factors. The strength will be directly proportional to the scattering factor for the respective peak, as per equation 14. Since it is a powder, diffraction will arise from multiple sets of planes, rather than just a single set of planes hkl for a certain plane spacing d_{hkl}. For example, looking at the planes of family 042, diffraction will occur for every set of planes in this family, e.g. [042], [024], [0$\bar{2}$4], and so on. For the family of 042, the degeneracy number will be 24, which means that there are 24 different sets of planes in this family, which will all have the same plane spacing. The diffracted signal for this diffraction angle θ will then be 24 times stronger than if we were to only consider one set of planes.

All of the experiments laid out in this thesis have been performed with a horizontally polarized X-ray beam. A horizontally polarised beam will make the electrons it interacts with oscillate in the same direction. The electrons will then, as discussed in chapter 3, emit dipole radiation, which is strongest in directions perpendicular to the polarization direction, and falls to zero in directions parallel to the polarization direction. The angular dependence of the intensity reduction is easiest to visualize in terms of the electric field. If we consider a particular scattering direction, and we imagine that we follow

this direction and look back at the dipole. Depending on the angle of the outgoing scattering direction, the projection of the dipole to the observation point will be shorter, and the decrease in viewed length of the dipole is directly proportional to the decrease of the electric field due to the angle.

If instead an unpolarized beam is used, another factor of $\frac{1+\cos^2(\theta)}{2}$, called the polarization factor for an unpolarized primary beam, will need to be added.

The pros of this measurement technique are that it can be used with a table-top X-ray setup, it is fairly easy to set up, and there are many commercial setups available, and it is possible to achieve very high resolution traces with respect to Q. The downside is that all of the signal is discarded except for a very narrow portion, and thus the signal strength is much weaker than if a large part of the 2-dimensional scattering information was captured. The angular information is also lost, for example the possibility to measure if the powder sample is structured, where larger domains with the same orientations have been created.

For the measurements on polycrystalline material in this work, where powder patterns have been recorded, a 2D detector has been used, and a large part of the scattering has been captured. To analyze this signal, the exact scattering geometry needs to be determined, that is, the distance from the sample to the detector, D, the tilt of the detector, the rotation of the detector R, and the photon energy, E. With all of these variables determined, the Q-value for every pixel on the detector is determined. The goal is to determine the average intensity for each Q-value, and get an intensity vs Q graph, as for the 1D case.

Before this can be calculated, however, each pixel needs to be normalized, both for the distance between that specific pixel and the interaction point with the X-rays and the sample, since the intensity falls of as $\frac{1}{R^2}$, and due to the polarization effects due to the horizontally polarized beam, as described by equation 5.

3.3 Diffuse scattering

In the previous sections, the focus has been on scattering from perfect lattices, where the scattered intensity is highly concentrated to areas close to the ideal Bragg spots. In reality, a crystal will never be a perfect lattice, excited phonon modes will always exist. Most commonly, these phonons are due to

thermal energy, but vibrations can also be introduced by optically exciting specific phonon modes. When vibrations are present, some of the scattered intensity will be located a significant distance from the Bragg spots [56]. This is known as diffuse scattering, and in an experiment it will appear as the name suggests, diffuse areas of scattered intensity that spans the whole range between the Bragg spots [57–59]. The diffuse scattering can be seen in the detector image in Figure 3.7. The scattering originates from a sample of indium antimonide (InSb). The sample has been rotated to de-tune from the resonance condition for Bragg scattering. There are still very bright spots visible, which is scattering very close to the sharp crystalline diffraction peaks. The scattered intensity which is not located closely around the Bragg reflections, most visible in between the Bragg spots, is the diffuse scattering [60–62].

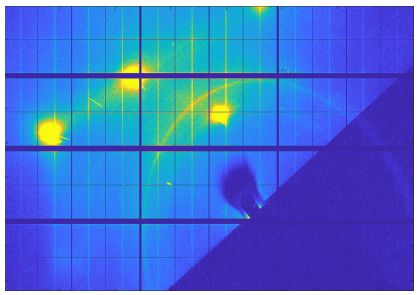

Figure 3.7: *Detector image of X-ray scattering from InSb. The experimental geometry has been tuned off from the resonant condition for Bragg scattering. The bright spots are areas close to the sharp Bragg reflections, and the scattered intensity between the Bragg reflections is the diffuse scattering.*

3.3.1 Theoretical background

We can consider the vibrations in a crystal as a linear combination of plane waves, with different directions, wavelengths, velocities and amplitudes. These waves will displace the atoms at positions x, y and z, a distance $u, v,$ and z. The geometry of the crystal and the crystal structure determines which wavelengths are allowed.

The most simple case to consider is a 1-D string of atoms, as shown in Figure 3.8. In a), the wavelength of the displacement vector is 4 times larger than the interatomic spacing a, however, in b), the wavelength is $1.5a$, which is identical to a wave with wavelength $3a$. This shows that wavelengths smaller than $2a$ can always be expressed as wavelengths greater than $2a$, and we thus only need to consider wavelength greater than twice the lattice spacing [63].

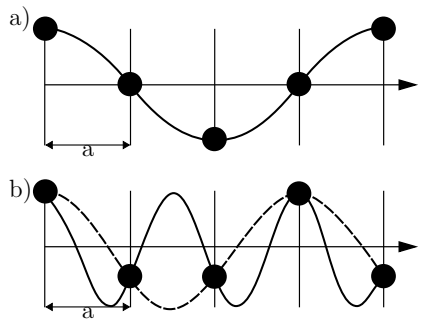

Figure 3.8: *Displacements of atoms in a one dimensional chain. a) The wavelength of the displacement vector is 4 times the atomic spacing a. b) The wavelength of the displacement vector is 1.5 times the atomic spacing a, this is identical to a wave with wavelength 3 times the atomic spacing.*

We can describe the plane waves with a propagation direction **g**, which has components **lmn** parallel to the principal directions of the crystal, and with vibration direction **e**, with components **ABC** parallel to the principal directions.

The displacement components can then be expressed as

$$\begin{aligned} u &= Aa\exp\left[(2\pi i/\Lambda)(Vt - lx - my - nz)\right] \\ v &= Ba\exp\left[(2\pi i/\Lambda)(Vt - lx - my - nz)\right] \\ w &= Ca\exp\left[(2\pi i/\Lambda)(Vt - lx - my - nz)\right] \end{aligned} \tag{19}$$

where a is the amplitude, Λ is the wavelength and V is the velocity.

When calculating the intensity of the diffuse scattering, it is useful to state the limitations of the wavelengths in terms of reciprocal space. For a cubic crystal, the first Brillouin zone is a cube centered at the origin with side lengths $\frac{1}{a}$, the above stated limitations are identical to stating that the wave-vectors of the plane waves must be confined to the first Brillouin zone, which can be expressed as

$$\begin{aligned} -\frac{a}{2} < g_x < \frac{a}{2} \\ -\frac{a}{2} < g_y < \frac{a}{2} \\ -\frac{a}{2} < g_z < \frac{a}{2} \end{aligned} \quad , \tag{20}$$

where g_x, g_y and g_z are the components of the wave vector in the x, y and z directions respectively.

Let us first consider the simplest case of a cubic, mono-atomic lattice, where we can express the normal stresses σ, and shearing stresses τ in terms of the normal strains ϵ, and the shear stresses γ as follows

$$\begin{aligned} \sigma_x &= c_{11}\epsilon_x + c_{12}\epsilon_y + c_{12}\epsilon_z \\ \sigma_y &= c_{12}\epsilon_x + c_{11}\epsilon_y + c_{12}\epsilon_z \\ \sigma_z &= c_{12}\epsilon_x + c_{12}\epsilon_y + c_{11}\epsilon_z \\ \tau_{yz} &= c_{44}\gamma_{yz} \\ \tau_{zx} &= c_{44}\gamma_{zx} \\ \tau_{xy} &= c_{44}\gamma_{xy} \end{aligned} \quad , \tag{21}$$

where c_{44}, c_{11} and c_{12} are three elastic moduli [64]. Using the three stress equilibrium equations

$$\begin{aligned}\frac{\delta\sigma_x}{\delta x}+\frac{\delta\tau_{xy}}{\delta y}+\frac{\delta\tau_{zx}}{\delta z}&=\rho\frac{\delta^2 u}{\delta t^2}\\ \frac{\delta\sigma_y}{\delta y}+\frac{\delta\tau_{xy}}{\delta x}+\frac{\delta\tau_{yz}}{\delta z}&=\rho\frac{\delta^2 v}{\delta t^2}\\ \frac{\delta\sigma_z}{\delta z}+\frac{\delta\tau_{zy}}{\delta y}+\frac{\delta\tau_{zx}}{\delta x}&=\rho\frac{\delta^2 w}{\delta t^2}\end{aligned}\quad , \tag{22}$$

where ρ is the density, together with Eqs. 20 and 21, the solutions are three possible distinct waves for each propagation direction g. If we consider the simplest case, waves propagating in the [100] direction, we get the three solutions

$$v_1^2 = c_{11}/\rho, \qquad A_1 = 1, \qquad B_1 = 0, \qquad C_1 = 0 \tag{23}$$
$$v_2^2 = c_{44}/\rho, \qquad A_2 = 0, \qquad B_2^2 + C_2^2 = 1 \tag{24}$$
$$v_3^2 = c_{44}/\rho, \qquad A_3 = 0, \qquad B_3^2 + C_3^2 = 1 \tag{25}$$

In this case, the first solution is a pure longitudinal wave, and the two other solutions are pure transverse waves. The two transverse solutions are identical, and any mutually perpendicular directions perpendicular to the propagation direction can be chosen.

For any other propagation direction, the three waves will still be independent, but they are not necessarily pure longitudinal or pure transverse waves, and the solutions are slightly more complicated.

As we did previously, we define the positions of atom n with the vector $\mathbf{r}_n = n_1\mathbf{a}_1 + n_2\mathbf{a}_2 + n_3\mathbf{a}_3$ and we let each wave with wave vector $\mathbf{g}$ have displacement directions $\mathbf{e}_j$. The displacements of atom n due to a wave gj can then be written as

$$\mathbf{u}_n(gj) = a_{gj}\, e_{gj} \cos(\omega_{gj} t - 2\pi\mathbf{g}\cdot\mathbf{r}_n - \delta_{gj}) \tag{26}$$

Using the convention $k = 2\pi/\lambda$ and $\mathbf{S}$=$\mathbf{s}$-$\mathbf{s}_0$, the scattered intensity is

$$I_{eu} = f^2 \sum_m \sum_n e^{ik\mathbf{S}\cdot(\mathbf{r}_m - \mathbf{r}_n)} \tag{27}$$

If we now include the displacements due to vibrations and replace $\mathbf{r}_m$ with $\mathbf{r}_m + \mathbf{u}_m$, the intensity becomes

$$I_{eu} = f^2 \sum_m \sum_n e^{ik\mathbf{S}\cdot(\mathbf{r}_m - \mathbf{r}_n)} e^{ik\mathbf{S}\cdot(\mathbf{u}_m - \mathbf{u}_n)} \tag{28}$$

We can substitute in

$$p_{mn} = k\mathbf{S} \cdot (\mathbf{u}_m - \mathbf{u}_n) \tag{29}$$

to get the time averaged scattered intensity

$$I_{eu} = f^2 \sum_m \sum_n e^{ik\mathbf{S}\cdot(\mathbf{r}_m - \mathbf{r}_n)} e^{ip_{mn}} \tag{30}$$

Since what is detect in scattering experiments is the average scattered intensity, we can simplify the calculations by instead looking at the time averaged amplitudes squared, $\langle a_{gj} \rangle$. If we also make the assumption that the waves are harmonic oscillators, and that there is a thermal distribution of amplitudes, we can write the scattering as

$$I_{eu} = f^2 e^{-2M} \sum_m \sum_n e^{(2\pi i/\lambda)\mathbf{S}\cdot(\mathbf{r}_m - \mathbf{r}_n)} e^{\sum_{gj} \cos 2\pi \mathbf{g}\cdot(\mathbf{r}_m - \mathbf{r}_n)} \tag{31}$$

where

$$*G_{gj} = \frac{1}{2}(k\mathbf{S} \cdot \mathbf{e}_{gj})^2 \left\langle a_{gj}^2 \right\rangle \tag{32}$$

and

$$2M = \sum_{gj} G_{gj} \tag{33}$$

is the exponent for the reduced intensity of the crystalline peaks due to the Debye-Waller factor [65, 66].

Using a Taylor expansion to the second term we finally get the equation [67]:

$$I_{eu} = f^2 e^{-2M} \sum_m \sum_n e^{(2\pi i/\lambda)\mathbf{S}\cdot(\mathbf{r}_m - \mathbf{r}_n)} \tag{34}$$

$$+ f^2 e^{-2M} \sum_m \sum_n e^{(2\pi i/\lambda)\mathbf{S}\cdot(\mathbf{r}_m - \mathbf{r}_n)} \sum_{gj} G_{gj} \cos 2\pi \mathbf{g} \cdot (\mathbf{r}_m - \mathbf{r}_n) \tag{35}$$

$$+ f^2 e^{-2M} \sum_m \sum_n e^{(2\pi i/\lambda)\mathbf{S}\cdot(\mathbf{r}_m - \mathbf{r}_n)} \left[\sum_{gj} G_{gj} \cos 2\pi \mathbf{g} \cdot (\mathbf{r}_m - \mathbf{r}_n) \right]^2 \Big/ 2 \tag{36}$$

Where the first term, the zero order term, describes the Bragg reflections, the second term is the first order temperature diffuse scattering, and the last term is the second order temperature diffuse scattering [67].

3.3.2 Simulating diffuse scattering

To analyze experimental TDS data, it is very useful to be able to conduct simulations with the exact scattering geometry used in the experiments. The experimental data shown in Figure 3.7 is diffuse scattering from a sample of InSb. The first logical step in performing simulation is to place the Detector in the correct location in 3D space. The detector used in this experiment is a Dectris Pilatus 1M, this detector has dimensions 1475x831 pixels with a pixel size of 172µm. The detector was located 125mm from the interaction point of the sample and had a tilt of 30 degrees in the scattering plane. To know which part of the scattered intensity will fall into which pixels, the detector pixels can be projected onto the Ewald's sphere as defined in Section 3.1.5. This is shown in Figure 3.9, where the black rectangle is the detector, the black shell is the detector pixels projected onto the Ewald's sphere, the blue arrows point in the direction of the incoming X-rays, where the shorter one indicates the magnitude of the incoming wave vector $\mathbf{k}_{in}$, and the longer one is extended to meet the detector, and the yellow arrow indicates the scattering direction for the scattering from the [100] planes.

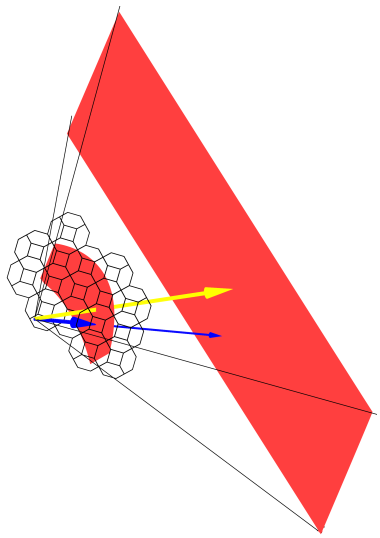

Figure 3.9: *The simulated detector shown as a red rectangle, with its projction onto the Ewald's sphere shown as a red shell. The blue arrows point in the direction of the incoming X-rays and the yellow arrow point in the direction of the scattering from the [100] planes.*

To know where in the Brillouin zones the scattering is coming from, the Brillouin zone for InSb has to be constructed. In the previous section we looked at the simpler case of a cubic unit cell, InSb has a zinc-blende structure with a fcc lattice structure. The Brillouin zone for such a lattice is a truncated octahedron which can be seen in Figure 3.10 a). This Brillouin zone can be copied and translated to fill the region in reciprocal space where the Ewald's sphere lies, this is shown in Figure 3.10 b), where the pixels on the detector have now been color coded depending on which Brillouin zone the corresponding points on the Ewald's sphere reside in.

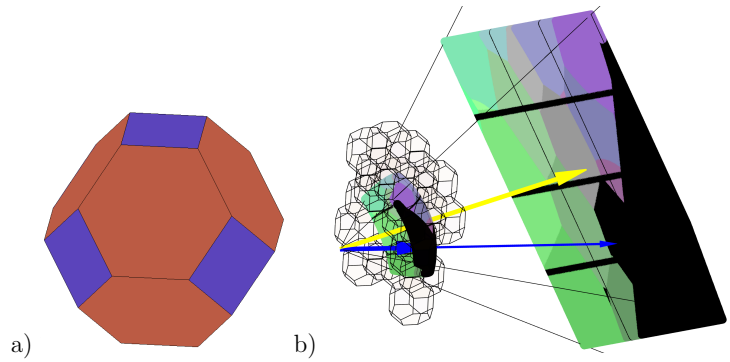

Figure 3.10: *a) The truncated octahedron which describes the first Brillouin zone for the fcc crystal structure. b) The Brillouin zones which the back-projected part of the Ewald's sphere lie in have been added, and the pixels on the detector have been color coded depending on which Brillouin zone the corresponding part of the Ewald's sphere lie in.*

When it is known which Brillouin zone every relevant point on the Ewald's sphere lies in, the points on the Ewald's sphere can be reduced to the first Brillouin zone. This means that for each Brillouin zone, the translation vector of the Brillouin zone is subtracted from the position vector of each point on the Ewald's sphere which lie in the corresponding Brillouin zone.

The formalism laid out in Equation 36 can now be used for each of these sampled points within the first Brillouin zone.

Figure 3.11: *The simulated diffuse scattering intensities using first order TDS.*

The result of the simulation using the zeroth and first order terms is shown in Figure 3.11.

Chapter Summary

The wave nature of X-rays, and their short wavelengths, allow X-rays to be diffracted in crystalline materials. X-ray diffraction is a powerful technique used for investigating solids. This chapter gives a theoretical overview for the mechanisms of X-ray diffraction. The next chapter discusses light interaction with matter and outlines a few thermal and non-thermal processes.

Chapter 4

Light interaction with matter

This chapter discusses how light interacts with matter, with a primary focus on high intensity laser pulses interacting with semiconductors. When energy is deposited into solids, many material properties can be altered in ways that can be measured with X-ray diffraction. Several of these processes occurs on very short time-scales, on the order of picoseconds, which is usually referred to as ultrafast times-scales. The next chapter will outline the method for ultrafast X-ray diffraction. The beginning of this chapter discusses the phenomena of absorption, which is the basis for all of the mechanisms which will be discussed in the chapter. The dynamics of absorption is described in terms of carrier excitation, and following this, heating of the lattice due to interactions between the excited carriers and the lattice. The last part of the chapter details a few ultrafast material responses, such as non-thermal melting and amorphization, which are material phase changes that happen before the carriers have time to deposit their energy into the material lattice.

4.1 Thermal excitation

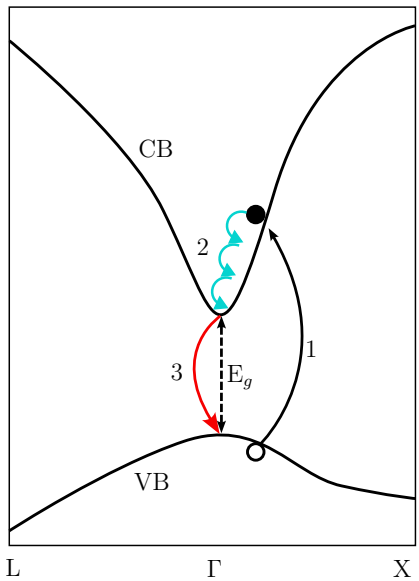

Figure 4.1: *Schematic three step process of the electron dynamics when a photon is absorbed by a semiconductor. 1) Excitation of an electron from the valence band to the conduction band, creating an electron-hole pair 2) Cascade of non-radiative decay events of a hot electron relaxing it to the bottom of the conduction band 3) Radiative decay of electron from the conduction band to the valence band, causing recombination of the electron-hole pair.*

When the photon energy has been absorbed by the electrons, all of the photon energy is initially stored in the electron system. For semiconductors, this means an excitation of an electron from the valence band, VB, to the conduction band, CB. This is shown as step one in Figure 4.1 [68]. If the excited electron sits higher in the conduction band, it can decay non-radiative to lower energies by transferring energy to the ions, depositing energy in the lattice system [69], which after a few tens of fs will result in thermal distribution of electrons in the conduction band [70–72].

The energy transferred to the ions will induce vibrations in the lattice, so-called phonons, and the specific phonons that arise from the non-radiative

decay are called Longitudinal Optical (LO) phonons [73]. If the phonons are created by intra-band non-radiative transistions as shown in the figure, the k-transfer from the electrons to the lattice will be small, since the momentum of the electron does not change very much. Thus, the resulting LO phonons reside close to the Γ point [74].

The creation of different types of phonons, which can have non-zero momentum, comes from the decay of the initial LO phonons. When the LO phonon decays into two Longitudinal Acoustic (LO) phonons, this is called the Klemen's decay channel [75]. The decay of LO into one Transverse Optical(TO) and one Transverse Acoustic(TA) phonon is called the Ridley-Gupta channel [76], and the decay from LO to one TA and one Longitudinal Acoustic (LA) phonon is called the Vallée-Bogani channel [77]. During each decay event, the energy and the phonon momentum q need to be conserved. The result of this is the generation of phonons with lower and lower energies, but not necessarily lower momentum, since the two generated phonons can have large, but opposite, momenta. After some time τ_{e-ph}, the electron phonon coupling time, most of the phonons will have decayed to low energy, low momentum, acoustic phonons.

4.2 Ultrafast phase transitions

When solid materials are irradiated with extreme x-ray intensities, ultrafast phase transitions can occur. The two types of ultrafast phase transitions considered in this thesis are non-thermal melting, and non-thermal amorphization, where interatomic bonds are broken due to high carrier excitation, allowing the crystalline structure to disorder before significant increase of the lattice temperature occur.

4.2.1 Melting

Thermal melting is the familiar melting process of matter going from a solid to liquid by adding heat to the material. This can be achieved either by letting the material be in thermal contact with a material at a higher temperature, for example by melting metal with a soldering iron, or by shining a light on an object. Following the previous section, exposing a material to light excites carriers, which lose energy to the ions in the material, making them vibrate more and more. When the mean square displacement of the atoms from their

equilibrium positions reach a fraction f of their interatomic distances a, where f is usually around 10% of the interatomic distance [78, 79], as stated in Lindemann's criterion

$$\frac{\sqrt{\langle u^2 \rangle}}{a} = f \quad , \tag{1}$$

the material will melt [80].

This is a comparatively slow process, in relation to ultrafast time scales, and depends on the electron-phonon coupling time, which is usually on the order of a few ps.

Non-thermal melting, on the other hand, is an ultrafast process, where the material melts before the electrons have time to transfer their excitation energy to the lattice. Let us again consider a semiconductor. At normal conditions, most of the electrons reside in the valence band, and there they assist in the atomic bonding of the material. When they are excited to the conduction band they are de-localized, and stop contributing to the bonding between atoms. Thus, when enough carriers are excited at the same time, the bonding forces that hold the solid together are too weak to overcome the thermal vibrational energy of the solid, and the solid undergoes a phase transition to a liquid, melting before the lattice has time to heat up.

The disordering time for the material is then mainly dependent on the thermal velocities of the ions at the instant of bond-breaking, since the ions will continue traveling at the velocity they had at that time. This model is refered to as the inertial model of non-thermal melting.

The most commonly used model to describe the heating dynamics of a metal after laser excitation is the two-temperature model

$$\begin{aligned} C_e \frac{\delta T_e}{\delta t} &= -G(T_e - T_l) + S(t) \\ C_l \frac{\delta T_l}{\delta t} &= G(T_e - T_l) \quad , \end{aligned} \tag{2}$$

where C_e and C_l are the heat capacities of the electrons and the lattice, respectively, G is the electron-phonon coupling constant and $S(t)$ is the time-dependent source term for the deposited energy. This model describes the heating as an initial depositing of the energy into the electron system, which

then transfers energy to the lattice system through electron-phonon interaction. When considering semiconductors on ultrafast timescales, it is necessary to separate the lattice system into an optical phonon system and an acoustic phonon system, using instead the three-temperature model

$$\begin{aligned} C_e\frac{\partial T_e}{\partial t} &= -G_{e-o}(T_e - T_o) \\ C_o\frac{\partial T_o}{\partial t} &= G_{e-o}(T_e - T_o) - G_{o_a}(T_o - T_a) \quad , \\ C_a\frac{\partial T_a}{\partial t} &= G_{o_a}(T_o - T_a) + k_a\frac{\partial^2 T_e}{\partial z^2} \end{aligned} \tag{3}$$

where C_e, C_{op} and C_{ac} are the heat capacities, and T_e T_{op} and T_{ac} are the temperatures for the optical and acoustic phonons, respectively, G_{e-op} is the coupling constant between the electronic and optical phonon systems, and G_{op-ac} is the coupling constant between the optical and acoustic phonon systems, defined as $G_{(e-o)} = \frac{C_o}{\tau_{e-o}}$ and $G_{(o-a)} = \frac{C_a}{\tau_{o-a}}$, τ_{e-o} and τ_{o-a} are the coupling times between the systems. and k_e is the heat conductivity of the acoustic lattice. In Equation 3 an additional heat conduction term is added to the lattice system, where k_a is the lattice thermal conductivity. This model describes the interaction as a three-level system, where the electronic system only interacts with the optical phonon system and the optical phonons subsequently decay into acoustic phonons, transferring energy from the optical phonon system to the acoustic phonon system. This extended model is required as the two phonon systems for a semiconductor, as opposed to a metal, cannot be viewed as a single system, since the coupling time constant between the two systems is non-negligible compared to the coupling time between the electronic system and the phonon system.

When experimentally investigating the non-thermal melting dynamics in semiconductors, the upper excited crystal layers will receive higher amounts of absorbed energy, due to the high optical absorption. Thus, even if sufficient fluence is used to cause non-thermal melting of the upper layers in the probing volume, the lower layers will instead undergo thermal melting, and these dynamics will be included in the recorded data. To fully describe the dynamics, the modeling needs to be depth dependent, where the behavior of the layers which are excited above the non-thermal melting threshold are treated using non-thermal melting dynamics, and the lower layers are described using the three-temperature model.

To model this behavior using Equation 3, the first step is to set the initial condition for the temperatures. When the material is excited, a high number

of carriers will be excited in the material, which will absorb light due to free carrier excitation. The absorption due to free carrier excitation can be modeled using a Drude mode, as $\alpha_{FCA} = 2k_0\sqrt{\left(\frac{\omega_p}{\omega_L}\right)^2 - 1}$, where ω_L is the laser angular frequency, and the plasma angular frequency is $\omega_p = \sqrt{\frac{ne^2}{\epsilon m_e^*}}$, where n is the excited carrier density, ϵ is the vacuum permittivity, e is the elementary charge and m_e^* is the electron effective mass. The electron effective mass will vary drastically with temperature due to the non-parabolic shape of the conduction band, and can be estimated using Kane's non-parabolic band model as $m_e^* = m_{eo}^*\left(1 - \frac{k_b T_e}{E_g}\right)$, where k_b is Boltzmann's constant, T_e is the temperature of the electron system and E_g is the band gap. The heat capacity of the electron system is assumed to be $\frac{3}{2}\mathrm{k_b}$ n where n is the excited carrier density. For the simulations it is assumed that every photon that is absorbed due to the linear absorption excites one carrier, and the photons that are absorbed due to free carrier absorption deposit their energy to the electron system without exciting any carriers. To calculate the initial temperature distribution and the initial carrier density, the depth of the crystal is divided up into small layers, and the energy is deposited in small chunks, where for each chunk of energy the number of excited carriers is calculated, which affects the absorption coefficient and the electron heat capacity. These updated values are used to calculate the absorption for the next chunk of energy, and the transmitted photon flux is used to calculate the heating and carrier excitation of the next layer. Typical initial carrier densities are shown in Figure 4.2.

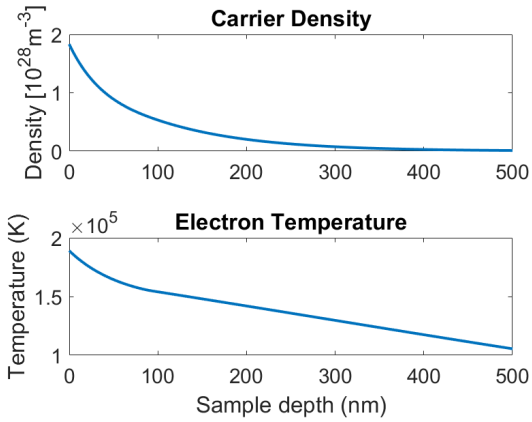

Figure 4.2: *Initial electron temperature and carrier density with 50 mJ/cm^2 excitation fluence.*

The temperatures of the three systems are then calculated by numerically solving Equation 3 using simple forward Euler method for the coupling terms and a Crank-Nicholson (CN) time-stepping scheme for the thermal conductivity in the lattice system. The carrier density is also evaluated using CN time-stepping, solving the diffusion equation, and updating the electron heat capacity each time step. The simulations results for the electron temperature, T_e, the optical phonon temperature, T_o, the acoustic phonon temperature, T_a, and the excited carrier density, n, over 15 ps, and a depth of 500 nm, are shown in Figure 4.3.

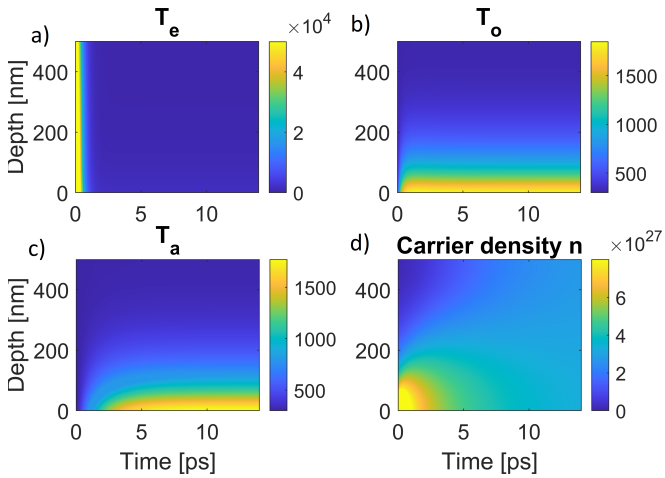

Figure 4.3: *Maps showing the time evolution of the simulations after excitation; a) The temperature of the electron system, b) The temperature of the optical phonon system, c) The temperature of the acoustic phonon system, d) The excited carrier density.*

The layers that reach an initial carrier excitation of over 10% of the total valence electrons undergo non-thermal melting. At the moment of bond breaking the atoms will continue to travel with their initial temperature vibrational velocities, and the reflected X-ray intensity from these layers are modeled as decreasing with a gaussian function, using the inertial model [81], as

$$I(t) = I(0)e^{-(t/\tau)^2} \tag{4}$$

where $I(0)$ is the incoming X-ray intensity, and τ is the room temperature disordering time, which has been shown by Wang *et al.* to be 470 fs [82]. As the acoustic phonon temperature of the layers reach the melt temperature of 800 K, the temperature increase stops until enough heat is deposited to overcome the latent heat of fusion, after which the temperature increase continues. In Figure 4.4 the red area indicates layers that have reached the melting point, but not overcome the latent heat of fusion.

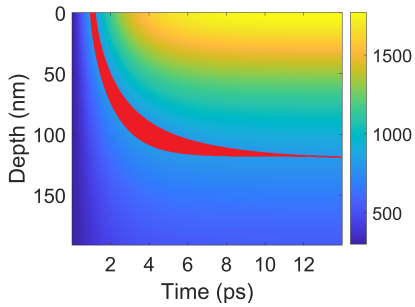

Figure 4.4: *Temperature map of the acoustic phonon temperature after excitation of 50 mJ/cm^2. The red area indicates layers that have reached the melting point, but not yet overcome the latent heat of fusion.*

As enough heat has been deposited to overcome the latent heat of fusion, the layers are considered molten, and the X-ray diffraction intensity from these layers are set to zero.

These simulations were performed to explain ultrafast X-ray diffraction data, where the top layers are melted non-thermally, and layers deeper into the film are thermally molten. Diffraction data together with simulation for excitation with a fluence of 50 mJ/cm^2 is shown in Figure 4.5.

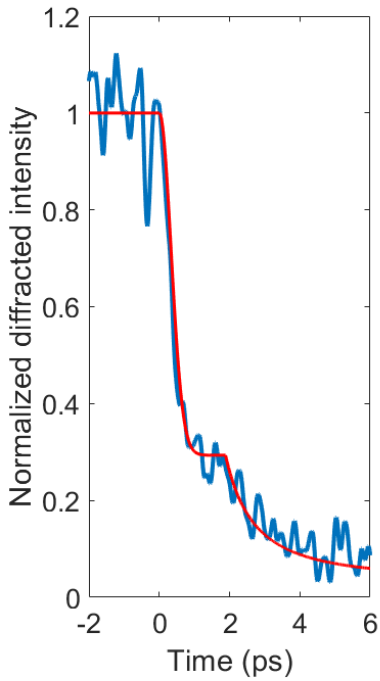

Figure 4.5: *Diffraction data with simulation after excitation with a fluence of 50 mJ/cm^2.*

The initial fast drop is due to non-thermal melting with a time constant of 470 fs, following this, there is a short plateau, due to the time it takes for the energy to decay into the acoustic phonon system, and for the temperature of the acoustic system to reach the melting point and overcome the latent heat of fusion. Subsequently, a slower decay is present due to deeper layers thermally melting.

4.2.2 Amorphization

Ultrafast amorphization of PCM materials, such as GST, has been the subject of considerable study for the past two decades. This would entail inducing a non-thermal phase shift from crystalline to amorphous, without melting

the material first, as is usually done. If this could be realized, it would mean significant speedup compared to conventional models. There have been a significant amount of studies conducted using pump-probe techniques to understand the initial response of GST after laser excitation, to understand the possible paths for non-thermal amorphization. This will be discussed in detail in chapter 6.5.2.

Chapter Summary

This chapter discusses how light interacts with matter, and how energy is deposited in solid materials. First, the incident light excites carriers, which can interact with the lattice and excite optical phonons, which in turn can decay into acoustic phonons, heating the lattice. Non-thermal melting and amorphization is discussed, where phase changes takes place before significant energy transfer to the lattice. The next chapter will discuss the method of time resolved X-ray diffraction.

Chapter 5

Time-resolved X-ray diffraction

To understand the mechanisms governing the transient material responses to photo-excitation, it is crucial to be able to measure the dynamics on the ultrafast timescale. Since many processes, such as optical phonons and non-thermal phase changes, occur on the picosecond timescale, a time resolution on the same time scale is necessary to fully be able to resolve the, sometimes, complex

Using time-resolved X-ray diffraction techniques can be used to monitor the transient response of different materials, such as metals, semi-conductors and protein crystals after laser excitation. Several ground-breaking observations have emerged from this research field, such as that of laser induced coherent acoustic phonons [83, 84], non-thermal melting of semiconductors [18, 81, 85, 86], and more recently that of laser-induced optical phonons [87], non-equilibrium phonon-distributions from measuring diffuse scattering [88, 89], insulator to metal transitions in quantum materials [90, 91], liquid-to-liquid phase transitions in phase-change materials [92], exciton-polaron driven lattice distortions in perovskites [93], and THz driven spin dynamics [94].

5.1 Pump-probe

Ultrafast x-ray diffraction experiments are conducted using pump-probe setups, where the probe is a sub-ps x-ray pulse, and the probe is usually a femtosecond laser pulse. The work presented in this thesis has been conducted using laser pump x-ray probe techniques. The experiments presented in papers I, II and IV, were conducted using a repetitive pump-probe setup, where the same part of the samples were excited and probed for each acquisition, whereas the results presented in paper III used a single-shot setup, due to single shot destruction of the sample, requiting a new sample position for each acquisition.

5.1.1 The FemtoMAX beamline

All experiments in this work were conducted at the FemtoMAX beamline at MAX IV. The FemtoMAX beamline is an ultrafast time resolved beamline at the MAX IV facility in Lund, Sweden, where it is possible to conduct laser pump/X-ray probe, scattering, experiments with a few femtosecond resolution.

The X-ray generation process starts nearly 400 meters before the FemtoMAX X-ray hutch, where a short pulse UV-laser creates free carriers through photoelectric excitation in a cathode. The bunch of electrons that is released is then accelerated using an RF-acceleration cavity to an energy of 3GeV. To be able to deliver short X-ray pulses, the bunch is compressed using two bunch compressers, and the compression can be down to a few femtoseconds. To generate X-rays, the electron bunch travels through two 5 meter long undulators, with 333 periods each. Between the undulators is a phase shifter to be able to delay the electron bunch so the two undulators add their radiation in phase. After the undulators, the electron beam path is deflected into the electron beam dump, and the X-rays continue into the FemtoMAX experimental hutch.

In the hutch the X-rays are focused with a bendable toroidal mirror. The smallest achievable beam size at the sample position is about 60 times 60 μm. At this point in the beamline, the spectrum is a very broad undulator spectrum. For the scattering experiments performed at the FemtoMAX beamline, a narrow bandwidth is required. For different studies we have chosen to utilize either the double crystal monochromators(DCM), or one of the multilayer monochromators [95].There are two different DCMs, one silicon DCM, which provides a bandwidth, $\frac{\Delta E}{E}$, of $2 \cdot 10^{-4}$ and an indium

antimonide DCM with a bandwidth of $4 \cdot 10^{-4}$, yielding a flux of $2 \cdot 10^5$ and $4 \cdot 10^5$ photons per pulse respectively [96]. The multilayer monochromator has a much wider bandwidth of 1%, and provides about 10^7 photons per pulse. When designing an experiment it is necessary to make a trade-off between high spectral resolution and high flux.

5.2 Timing monitor

The experiments conducted in this work, and generally in the field of ultrafast X-ray diffraction, are carried out with sub-ps time-resolutions. The accuracy which is necessary depends on the time-scales associated with the phenomenon of interest. For example, optical phonons can have frequencies exceeding 15 THz, which means that a time resolution of around 30 fs is needed to resolve the oscillations.

At beamlines such as FemtoMAX, the shot-to-shot timing jitter exceeds the time-resolution needed for most experiments, and without a way to mitigate this, experiments needing time-resolutions on this scale would not be feasible. The method to overcoming this is post-sorting. By saving timing information together with each detector image, the data can be sorted, and the limitation on the time-resolution is now the time-resolution of the timing tools used to determine the timing information, not the jitter. At the FemtoMAX beamline, two timing tools are used. The ping-monitor for rough timing (200 fs), and the cross-correlator for finer resolution (30 fs).

5.2.1 Ping monitor

For coarse post-sorting of the timing at FemtoMAX, an RF based monitor is used, which is referred to as the ping monitor. This device measures the relative timing between the laser, which is used as pump in the pump-probe experiments, and the electron bunch which generates the X-rays. After the electron bunch passes through the two 5 meter long undulators, it is deviated by a bending magnet, and led to a beam dump. The electron bunch is intrinsically synchronized to the generated X-rays, which are used as probe in the experiments. Thus, the timing between the electron bunches and the laser pulses can be used to monitor the shot-to-shot timing jitter.

An RF antenna has been placed between the undulators and the electron

beam dump. A voltage is induced when the electrons pass the antenna. On the laser end, parts of the pulses in the diagnostics arm are measured with a fast photodiode. These signals are then together sent through a 6 GHz bandpass filter. The output after the filter is an oscillating signal, where the oscillations depend on the relative phase between the signal from the electrons and the signal from the laser. This signal is measured by a fast oscilloscope, and using a Hilbert transform based algorithm, the relative timing can be calculated.

The ping monitor has been shown to provide an accuracy of 200 fs. What makes the ping monitor useful is that it provides a very large range, of hundreds of nanoseconds, for measuring the relative timing between the X-rays and the laser, without any additional adjustments. The standard method to find the timing for the simultaneous arrival of the two pulses at FemtoMAX, is to first measure the coarse timing with a photodiode. This coarse measurement is accurate to around 100ps. The next step is to conduct pump probe measurements, using a well known sample with a fast response (<100 fs), usually bismuth [87]. This is a standard experiment at the beamline, and the timing between the two pulses is scanned within this 100 ps time range to find the relative timing between the pulses for the fast response. It is thus very useful to have a timing monitor with a large range to be able to scan the entire time range without having to make any adjustments.

Furthermore, in many experiments conducted at FemtoMAX, the dynamics at longer times are of interest, for example to study regrowth dynamics or heat transfer, where the dynamics of interest can span 100s of nanoseconds. For such long dynamics, the resolution of 200 fs is more than sufficient.

5.2.2 Cross-correlator

The post-sorting for finer time resolution at the FemtoMAX beamline is done using a cross-correlator setup. This scheme uses a small fraction of the diagnostics beam and white light generated at the bending magnet. The two beams are focused vertically using cylindrical lenses and mixed at an angle of 12 degrees in a sum frequency generation crystal. The light that is generated by mixing one photon from each beam will travel in the forward direction, as is seen in Figure 5.1.

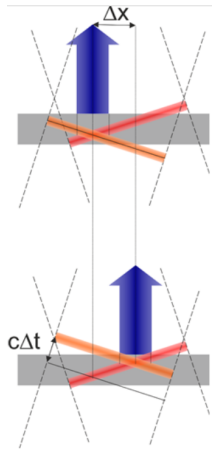

Figure 5.1: *Schematic overview of the cross-correlator timing measurement. The red pulses are the incoming diagnostics laser pulse and the white light pulse. The blue arrow indicates the position of the light generated by mixing the two incoming pulses. A change in relative delay of $c\Delta t$ between the incoming pulses moves the mixed signal a distance Δx.*

Depending on the relative delay between the diagnostics pulse and the white light pulse, the generated pulse will have a different sideways position, Δx, which is used to determine the delay. The size of the window is

$$\Delta X = \frac{c \cdot t_{cc}}{n \sin(\beta/2)} \qquad (1)$$

where c is the speed of light, t_{cc} is the cross-correlation width, n is the refractive index, and β is the relative angle between the two beams.

The geometry of the cross-correlator setup at the FemtoMAX beamline allows for a cross-correlation width of about 6 ps. This is a narrow window, especially when comparing to the unlimited window for the ping monitor. The upside is the drastically improved time resolution. Whereas the ping monitor has a resolution of about 200 fs, the cross-correlator has a resolution of less than 70 fs.

Chapter Summary

Several material responses to laser excitation takes place during ultrashort timescales, on the order of ps. Time resolved X-ray diffraction is a powerful technique for investigating transient responses in solids. This chapter discusses the technique of TRXRD, and how to achieve fine time-resolution by post-sorting. The next chapter will discuss different models for explaining the ultrafast response of GST after laser excitation.

Chapter 6

Experimental work

This thesis is based is based on ultrafast x-ray studies of the excitation response of InSb and $Ge_2Sb_2Te_5$. This chapter discusses the results presented in article II and article IV, where the sub-ps and few ps dynamics of the diffraction peaks in $Ge_2Sb_2Te_5$ are investigated, and models describing the transient excitation responses are presented. The chapter also presents the study conducted in paper III on the transition between thermal and non-thermal melting of InSb, and also an ongoing study on the ultrafast excitation of zone-boundary phonons in InSb.

6.1 Diffuse scattering from Indium Antimonide

We have conducted experiments investigating the ultrafast response of the diffuse scattering in indium antimonide (InSb) after laser excitation. In chapter 2.2 the theory of X-ray scattering for a perfect crystal was discussed, and the formalism mainly considered a single crystalline reflection at a time. Inspecting the 2D Ewald's sphere in Figure 3.5, it can be seen that the scattering condition can be fulfilled for multiple crystalline reflections at once, and that the reflections will be scattered from the sample at different scattering angles. In the experiments we used single crystalline InSb wafers that were cut with a 20°angle from the (111) direction towards the (110) direction. Using a sample with a surface which is not parallel to the crystal planes, one can by rotating the crystal around the surface normal to satisfy the scattering condition for different crystalline reflections. In the section

on diffuse scattering, it was explained that diffuse scattering can arise due to thermal motion in the crystal, where interaction between the X-rays the acoustic phonons impart additional momentum to the outgoing X-rays, which causes the diffuse scattering to exit the sample with a slightly different angle than the corresponding Bragg reflection. Close to the Bragg peaks, the main contribution is due to the first order diffuse scattering, which is the strongest contributing term. The further from the Bragg peaks, the weaker the diffuse scattering signal becomes. Here, higher orders of diffuse scattering contribute to a higher degree. When considering the reciprocal space view, the scattering from a perfect lattice can be seen as the points where the Ewald's sphere cut through the Γ point of the Ewald's sphere. The aim of this study was to measure the phonon excitation near the Brillouin zone edges due to photo-excitation, so called zone-boundary phonons, specifically at the zone boundary along the high symmetry K-direction.

When planning this experiment, we used a modified version of the script discussed in chapter 3.3.2. In this extension, additional data was stored in each simulated detector pixel. Each detector pixel in the simulation correspond to a specific location on the Ewald's sphere, and by extension, one specific outgoing scattering angle from the sample. The first information additional information that is calculated is which Brillouin zone the corresponding point on the Ewald's sphere reside in for each detector pixel, and the second information is how far that point on the Ewald's sphere is to the Γ point in the Brillouin zone in which it resides, and also how far the point is from the closest high symmetry vector, X or L.

Before the experiment, we conducted a series of simulations with X-ray energy 9 keV, where the azimutal angle of the sample was varied for each simulation. The purpose of these simulations was to find an azimutal angle where two crystalline reflections were visible where the position of the corresponding Brillouin zones were related by $[h_1, k_1, l_1] = [h_2 \pm 1, k_2 \pm 1, l_2 \pm 1]$, so the connecting high-symmetry line connecting the Brillouin zones is the K-line. This is shown in Figure 6.1, where the Ewald's sphere cut through the Γ points in the [0,4,0] and [1,3,1] Brillouin zones, which are connected along the [1, -1, 1] direction in reciprocal space. The strength of the yellow line connecting the two Γ points indicate how closely the corresponding points on the Ewald's sphere are to the connecting K line.

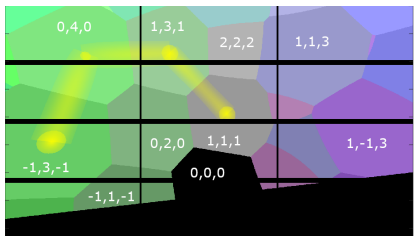

Figure 6.1: *Simulated detector image where each pixel is grouped depending on which Brillouin zone the corresponding point on the Ewald's sphere reside. The strength of the yellow circles indicate how close the point is to the corresponding* Γ *point, and the strength of the yellow lines indicate how close the point on the Ewald's sphere is to the connecting high symmetry line between the two* Γ *points.*

Since the aim was to investigate the point along the K-line which resides on the Brillouin zone boundaries, the goal of the simulations was to obtain an experimental configuration where the Ewald's sphere perfectly cuts through reciprocal space at this point. Further simulations were thus conducted, with the same azimuthal angle but varying the X-ray energy until this condition was met.

When setting up the experiments, the X-rays were tuned to an energy of 9 keV, as was used in the simulations. An grazing incidence geometry, at an angle of 0.4°was used. The resulting diffraction pattern was recorded on the Pilatus 1M detector, which is the detector that was emulated in the simulations, and the azimuth angle of the InSb sample was adjusted until the pattern resembled the simulated pattern. The scattering pattern on the detector, when the experiment is set up to resemble the simulations, is shown in Figure 6.2.

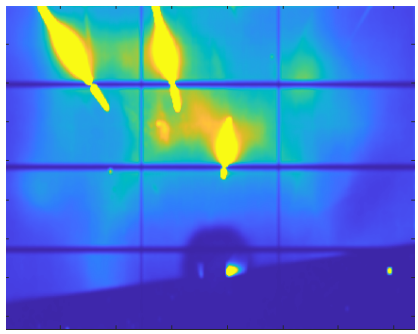

Figure 6.2: *Detector image of the scattering from InSb when the experimental setup is adjusted to mimic the settings used in the simulations, shown in Figure 6.1.*

The image is highly over-saturated to clearly show the diffuse scattering, especially along the high-symmetry K line between the two Bragg spots.

The sample was then excited using 800 nm laser radiation with a fluence of 35 mJ/cm^2. Scattering patterns were obtained both without laser excitation and at a delay of 1 ps after excitation, to investigate the ultrafast phonon distribution after excitation.

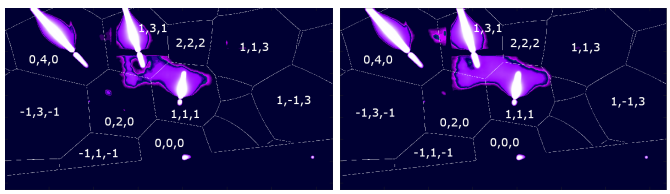

Figure 6.3: *Detector images of the scattering pattern of InSb. In the left figure is shown data taken before laser excitation and in the right figure is data taken 1 ps after laser excitation. The zone-boundary between the [0,4,0] and the [1,3,1] shows an increase in diffuse scattering after laser excitation.*

The proccessed data before and after laser excitation is shown in Figure 6.3, where the color scale is logarithmic to highlight the changes in the diffuse scattering. Comparing the diffuse scattering before and after laser excitation, the zone-boundary between the [0,4,0] and [1,3,1] zone boundary, where the Ewald's sphere cuts close through the high symmetry K line, shows an increase

in diffuse scattering after laser excitation. When diffuse scattering is present away from the direct Bragg reflections, the scattered X-rays have interacted with a phonon away from the Γ point in the Brillouin zone. This indicated that the increase in diffuse scattering at the zone-boundary can be due to an increase in the zone-boundary phonon population after laser excitation. Further analysis needs to be conducted to fully describe the phonon population after laser excitation.

6.2 Thermal and Non-Thermal Melting of InSb

Pump-probe experiments were conducted at the FemtoMAX beamline at the MAX IV synchrotron facility in Lund investigating non-thermal melting in InSb. A laser pump with a wavelength of 800 nm and a varying fluence between 30 and 70 mJ/cm^2 was used, which is sufficient for depositing enough heat in the sample to raise the temperature to the melting point of InSb, 800 K, and to overcome the latent heat of fusion. Due to high absorption in InSb, with a linear absorption constant of $10^7 \mathrm{m}^{-1}$, the energy density will vary drastically with sample depth. At the high end of the fluence range, over 10% of the carriers are excited in the top layers, causing bond-breaking.

The X-rays were incident at a grazing angle of 0.8 degrees, and the studied sample was an asymmetrically cut InSb wafer with a cut angle of 30 degrees from the [111] planes towards the [110] planes. Using an asymmetrically cut sample, the [111] reflection can be probed at grazing incidence to match the probe depth to the pump depth. To satisfy the scattering condition for the [111] reflection in this geometry, X-rays with energy 3.6 keV were used. The laser pump was incident at a 45 degree angle to the surface. The relative timing between the laser and X-rays will vary along the beam due to the difference in incidence angles, and the spatial information can be transformed into temporal information. The temporal dependence on the spatial coordinates is described by

$$t = L(\cos(\theta_{x-rays}) - \cos(\theta_{laser}))/c \tag{1}$$

where L is the position along the sample and $\cos(\theta_{x-rays})$ and $\cos(\theta_{laser})$ are the incident angles for the X-rays and laser. The experimental geometry is shown in Figure 6.4.

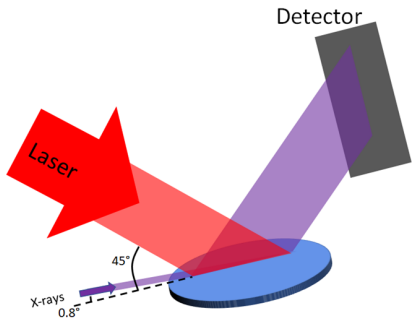

Figure 6.4: *The scattering geometry used for investigation of non-thermal melting in InSb. The laser is incident with angle 45 degrees and the X-rays with angle 0.8 degrees. Due to the asymmetrical cut, the X-rays will be scattered from the [111] planes with an angle of 60 degrees to the surface, which spatially stretches the outgoing X-rays vertically compared to the indicident X-rays.*

After re-crystallization, the excited material does not re-grow into a perfect crystalline lattice, and therefore a new sample position was used for each acquisition to ensure that all data was acquired with the same experimental conditions.

The intensity decrease of the [111] reflection was modeled by solving the equations described in 3, using initial conditions described in chapter 4.2.1, where the absorption is due to linear absorption and free-carrier absorption as described by the Drude model.

6.3 Ultrafast response of GST excitation

Conventionally, switching between phases of GST has been done by thermal melting, either using lasers or electric current. To initialize the bits to 0, GST is melted with a short pulse and allowed to quickly cool down, causing the material to solidify without having time to order into a crystalline structure. When writing a 1, a long, low-intensity pulse is used, increasing the temperature to above the crystallization temperature. This causes the atoms to order themselves into a crystal lattice, and the long pulse gives the material enough time to fully crystallize.

Recently, substantial effort has gone into research on neuromorphic computers, which are systems aimed to mimic the complex structure of the human brain for computing to increase the potential for parallel computing and to create a more adaptive data structure. Since the brain relies on neurons, which have a lot of connectivity, neuromorphic computers using 3D structures are very promising, which gives PCM an advantage over conventional computer infrastructure.

Currently, the pulses used for initializing the bits to 0 are on the order of 100 ns, and the pulses for writing 1 are on the order of 10 ns. This is slightly longer than the conventional read write cycles of DRAM.

In the past decade, numerous studies have explored non-thermal pathways for the amorphization of GST. This could improve the initialization time dramatically from the order of 10s of nanoseconds to the order of picoseconds, a factor of 10 000. Furthermore, the conventional method need to deposit enough heat into the material to facilitate melting, whereas non-thermal pathways could change the phase of the material while depositing significantly less energy. In addition to faster write speeds, this also drastically reduces the requirements for temperature control.

6.4 Combination of Previously Proposed Models

We have conducted ultrafast pump-probe experiments using x-ray diffraction to investigate the sub-ps response of GST. To explain the behaviour, we have also conducted x-ray diffraction simulations using previously proposed models of the ultrafast excitation response. As will be shown in the following section, none of the previously proposed models satisfies the intensity decrease of all

the measured peaks simultaneously. To fit the simulations to the data, we suggest that several of the proposed models occur simultaneously. First a reduction of the resonant bonding takes place in the first 100 fs, which is on the order of our experimental resolution. Following this, an umbrella flip of 15% of the Ge atoms take place during 3 ps, while at the same the neighboring Te atoms move in response to the new bonding structure, as proposed in the Te centric NMR study conducted by Sen *et al.* [97]

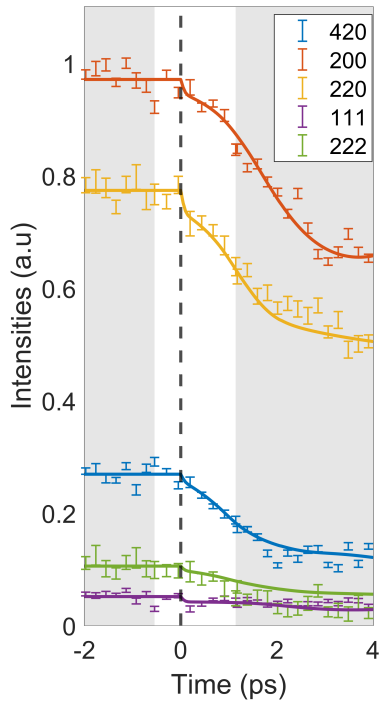

Figure 6.5: *Error bars show the X-ray diffraction data of the intensity of 5 diffraction peaks following laser excitation and the solid lines show simulation results for an initial suppression of the resonant bonding, with a subsequent umbrella flip over 3 ps.*

As seen in Figure 6.5, the combination of the previously discussed models very accurately fit the data. The following section shows that no one proposed

model can accurately fit the data for all of the peak intensities following laser excitation, and from Figure 6.5 we show that a more holistic combination is needed.

6.5 Previous studies

The research that has been conducted consist of simulation efforts and experimentally of pump-probe experiments with ultrafast laser and either laser or X-ray probes. At the moment of writing the scientific community has not yet reached consensus on the ultrafast material response after excitation, and several models have been proposed. These models include; direct ultrafast amorphization, which was suggested as the results of an electron diffraction study carried out by Waldecker *et al.* by following the intensity of the crystalline peaks [20]. A suppression of the Peierls distortion, which was suggested by Qi *et al.* following MD simulations and an electron diffraction study, where the intensity drops of the scattering peaks were modeled using monoexponential functions, which were thought to be due to the suppression of the distortion [19]. A rattling motion of the Ge atom, where the Ge atoms move in a circular orbit around their equilibrium positions in the lattice following excitation, which was suggested by Matsubara *et al.* to explain the changes in the intensity of the diffraction peaks in an X-ray diffraction study [21]. The reduction of resonant bonding following laser excitation was proposed as an initial response by Kolobov *et al.* following Charge Density Difference (CDD) simulations [98]. An initial motion of the Ge atoms along the (111) directions was proposed by Kolobov *et al.* [47]. This model suggests that the Ge atoms move from their octahedral position to their preferred tetrahedral position as a precursor to amorphization. This section will present these models and discuss how they fit to our experimental data.

6.5.1 Inverse Peierls Distortion

Qi *et al.* suggested that the intensity reduction of the diffraction peaks after excitation occurs due to a suppression of the initial Peierls distortion that is present in the equilibrium metastable rock-salt structure of GST. This was supported by Time-Dependent Density-Functional Theory Molecular Dynamic simulations (TDDFT MD) [19]. However, as is explained in the article, the structure factor for the even reflections, such as (200) and (220), increases with

a reduction of the Peierls distortion. Only the odd reflections, such as (111) and (311), show a reduction in intensity when suppressing the Peierls distortion. This is because the even reflections exhibit constructive interference between the Te and Ge(Sb) sub-lattices when the crystal is undistorted, whereas the odd reflections exhibit destructive interference, as shown in Eq 17. Thus, any deviation from a perfect rock-salt structure caused by moving the two sublattices with respect to each other will increase the intensities of the odd diffraction peaks, and decrease the intensity of the even peaks.

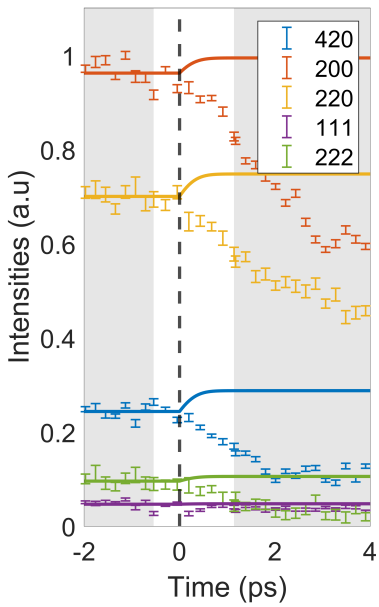

Figure 6.6: *Error bars show the X-ray diffraction data of the intensity of 5 diffraction peaks following laser excitation and the solid lines show simulation results for a initially Peierls distorted GST crystal with a suppression of the Peierls distortion over 0.7 ps.*

Our experimental data together with simulation results using an inverse Peierls distortion with a time constant of 0.7 ps is shown in Figure 6.6. As is seen in the Figure, the inverse Peierls distortion increases the intensity of all the even peaks, and is not sufficient to explain the intensity decrease.

6.5.2 Ultrafast amorphization

Ultrafast amorphization of crystalline GST after laser excitation was suggested by Waldecker *et al.* to explain the results of a conducted electron diffraction study [20]. In the study this was motivated by the decrease of the intensity of all the studied diffraction peaks, and by a broad peak around the (200) peak being visible 15 ps after excitation. Due to this being an electron diffraction study, the Q-resolution is limited, and it is difficult to discern between a reduction of the peak intensities and a broadening of the peaks, from amorphization. In our experimental data, we do not see signatures of amorphous scattering after excitation.

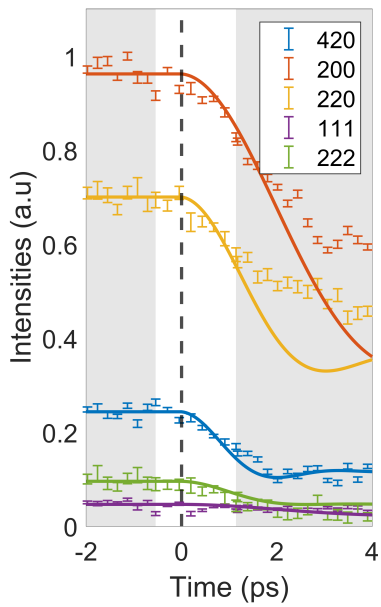

Figure 6.7: *Error bars show the X-ray diffraction data of the intensity of 5 diffraction peaks following laser excitation and the solid lines show simulation results where 30% of the atoms are given a random initial velocity.*

Our experimental data together with non-thermal amorphization simulations are shown in Figure 6.7. In the simulations 30% of the atoms have been given

random initial velocities, as for non-thermal melting. The fraction of the material being amorphized was chosen to be 30% to match the intensity drop of the (420) reflection. As can be seen in the Figure, the intensity drops due to non-thermal amorphization cannot simultaneously satisfy all of the studied peaks.

6.5.3 Umbrella Flip

The umbrella flip model as an initial motion before amorphization was proposed by Kolobov *et al.* [47]. This model suggests that the Ge atoms move in the (111) directions until they reach their new tetrahedral position. The magnitude of this motion is half the bond-length of the Ge-Te bonds. We have modeled the motion of the Ge atoms as a dampened sinusoidal, with an equilibrium position at the tetrahedral coordination position.

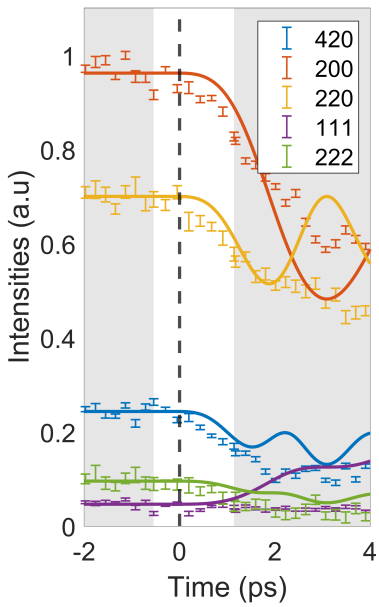

Figure 6.8: *Error bars show the X-ray diffraction data of the intensity of 5 diffraction peaks following laser excitation and the solid lines show simulation results for an umbrella flip motion of the Ge atoms.*

As seen in Figure 6.8, the shape of the simulations show similar signatures as the experimental data, but several features show large deviations from the data. The intensity increase of the (111) peak is severely overestimated, and none of the intensities closely follow the experimental results after 1 ps.

6.5.4 Suppression of Resonant Bonding

A suppression of the resonant bonding present in the A7 distorted GST after excitation was proposed by Li *et al.* [99]. It was shown experimentally by Shportko *et al.* that the crystalline structure of GST exhibits resonant bonding, which is not present in the amorphous structure [100]. We simulated the reduction of the resonant bonding by moving one from each Te location to the bonds.

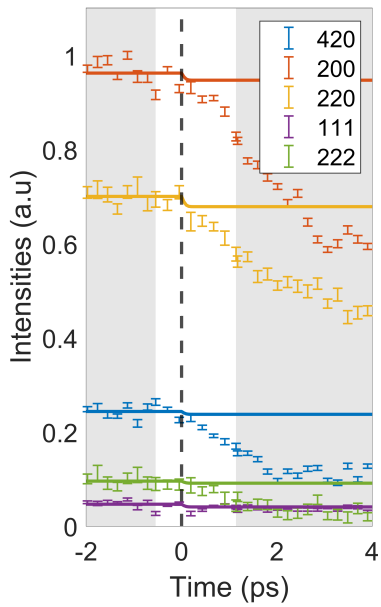

Figure 6.9: *Error bars show the X-ray diffraction data of the intensity of 5 diffraction peaks following laser excitation and the solid lines show simulation results for a fast reduction of the resonant bonding.*

In Figure 6.9 we see that the loss of resonant bonding lowers the intensity for each diffraction peaks. This quick initial intensity reduction closely matches the initial decrease of the (200) and (220) peaks. After this initial decrease, further effects need to be taken into account to match the intensities.

Chapter Summary

Ultrafast amorphization of GST has been extensively studied for two decades. Several experimental and simulation studies have been conducted, and different models explaining the ultrafast response of GST after laser excitation have been proposed. This chapter discusses some of these models, and compares these models to X-ray diffraction data. A conclusive model, combining a few of the mentioned models is presented, which more accurately describes the data.

Chapter 7

Summary and Outlook

Looking to the future, the newly commissioned cross-correlator for post-sorting of relative timing between x-rays and laser at the FemtoMAX beamline opens up exciting possibilities for new types of experiments that were previously not possible at the MAX IV facility. The results presented in paper II were obtained with this timing tool, which provided the necessary time accuracy to resolve the fast dynamics immediately after excitation. Further investigations into non-thermal effects in both conventional semiconductors and phase-change materials (PCMs), will require very fine time resolutions to distinguish sub-picosecond behavior from subsequent thermal processes, to thoroughly describe the full excitation dynamics.

The thermal effects, such as lattice heating and thermal melting, can be separated more accurately from the non-thermal effects using the models in paper III. The free-carrier absorption model reproduces the measured optical penetration depths, which is crucial for several experiments where the deposited energy density is non-uniform throughout the probe depth. The ability to calculate the actual fluence at each sample depth provides the possibility to conduct depth dependent simulations, where different mechanisms occur at different depths, thus obtaining a complete description of the experimental effects, with lower uncertainties due to lower laser intensity in the deeper layers. Combined with the accurate models describing the thermal evolution using the three-temperature model, experiments where the thermal effects deep in the sample are large compared to the ultrafast effects of interest are now feasible.

For further research into the non-thermal pathways for amorphization in PCM, such as $Ge_2Sb_2Te_5$, these advancements are crucial, where the parameters provided in paper IV for the Debye-Waller factors and electron-phonon coupling times are crucial to precisely determine the temperatures at different parts of the samples. The initial motions and bonding effects shown in paper II provide key insights to ultimately determine the mechanism behind ultrafast amorphization.

The Author's Contributions

I. A cross-correlator-based timing tool for FemtoMAX

In this paper, a cross-correlator technique for timing monitoring was built and tested. I planned and conducted the experiments for testing, analyzed the data and prepared figures and wrote parts of the manuscript, and provided comments on the rest of the manuscript.

II. Laser induced coherent atomic motion in GST

An X-ray diffraction study was conducted to study the ultrafast optical response of GST. I planned the experiments, jointly built the setup, conducted the experiments and acquired the data. I analyzed all the data and prepared the first draft of the manuscript.

III. The transition between Thermal and Non-Thermal Melting in InSb

In this study, the transition between thermal and non-thermal melting in InSb was investigated. I assisted in planning the experiments, conducting the experiments and assisted during data analysis. I developed the simulation code and conducted the simulations, and prepared parts of the manuscript.

IV. Approximation of Debye-Waller factors and electron-phonon coupling time in the phase-change material $Ge_2Sb_2Te_5$

By simultaneously evaluating the thermal expansion and the decrease in X-ray scattering intensities, Debye-Waller factors for high temperature GST were measured. I planned the experiments, jointly built the setup, conducted the experiments and acquired the data. I also assisted with data analysis.

Acknowledgments

I would like to thank my main supervisor Prof. Jörgen Larsson for all the knowledge shared, for all the long discussions, the guidance and moral support during stressful beamtimes, and for helping me reach this milestone.

I would also like to thank my co-supervisor Dr. Olle Lundh for you support and for always keeping your door open.

I want to thank my previous colleague Åsa for showing me the ropes, for all the soulful discussions about art, music, philosophy and so much more during the dark night hours in the FemtoMAX basement.

Thank you Carl Ekström for always being helpful, never complaining no matter how annoying my requests are, for always being a bright light. Without your unending assistance I would never have managed to finish a single experiment.

Andrius Jurgilaitis, thank you for your unlimited patience. I might be the most annoying user, but you taught me almost everything I know about the beamline, and without you I would never have the competence to ask all the annoying questions.

David Kroon, thank you for all the scientific discussions during beamtimes, for teaching me about timing and lasers, and also for a couple of car rides home.

Thank you Thai Van Pham for your diligence, for keeping tabs on the details, and allowing the experiments to work, and thank you for always being of assistance when I call when there is a crisis at FemtoMAX.

I also want to thank Xiaocui Wang for welcoming me into the group, Isa Clemensson for all of the critical questions keeping me on my toes, Byungnam

Ahn for helping with the laser and providing heating for our samples, Erik and Filip, and the whole accelerator team for providing us with nice electrons and listening to our requests, and also the wonderful floor coordinators for helping me so I could sometimes get a few hours of sleep.

Thank you to the division of Atomic Physics, you are all wonderful colleagues, and together you work to provide a friendly welcoming atmosphere, rich with love and stimulating conversation.

A special thanks to Anders Persson for always being helpful and patient, and helping me figuring out creative solutions to new problems.

Thank you Ella for the beautiful cover art.

Finally, I would like to thank all my friends and family for providing moral support, distraction, a shoulder to cry on, and so much more. Without you I would have never managed.

References

1 W. H. Bragg and W. L. Bragg. “The Reflection of X-rays by Crystals”. In: *Proceedings of the Royal Society A: Mathematical, Physical and Engineering Sciences* 88.605 (1913), pp. 428–438.

2 F. Horiguchi. “Advanced memory concepts for DRAM and nonvolatile memories”. In: *Solid-state electronics* 50.4 (2006), pp. 545–550.

3 P. Pavan, R. Bez, P. Olivo and E. Zanoni. “Flash memory cells-an overview”. In: *Proceedings of the IEEE* 85.8 (2002), pp. 1248–1271.

4 T. Hara, K. Fukuda, K. Kanazawa, N. Shibata, K. Hosono, H. Maejima, M. Nakagawa, T. Abe, M. Kojima, M. Fujiu et al. “A 146 mm/sup 2/8 Gb NAND flash memory with 70 nm CMOS technology”. In: *ISSCC. 2005 IEEE International Digest of Technical Papers. Solid-State Circuits Conference, 2005.* IEEE. 2005, pp. 44–584.

5 I. Bhati, M.-T. Chang, Z. Chishti, S.-L. Lu and B. Jacob. “DRAM refresh mechanisms, penalties, and trade-offs”. In: *IEEE Transactions on Computers* 65.1 (2015), pp. 108–121.

6 S.-K. Park. “Technology scaling challenge and future prospects of DRAM and NAND flash memory”. In: *2015 IEEE international memory workshop (IMW)*. IEEE. 2015, pp. 1–4.

7 J. S. Meena, S. M. Sze, U. Chand and T.-Y. Tseng. “Overview of emerging nonvolatile memory technologies”. In: *Nanoscale research letters* 9.1 (2014), p. 526.

8 S.-P. Yang, M. Kim, S. Nam, J. Park, J.-Y. Choi, E. H. Nam, E. Lee, S. Lee and B. S. Kim. “Overcoming the memory wall with {CXL-Enabled}{SSDs}”. In: *2023 USENIX Annual Technical Conference (USENIX ATC 23)*. 2023, pp. 601–617.

9 T. Matsunaga and N. Yamada. “Crystallographic studies on high-speed phase-change materials used for rewritable optical recording disks”. In: *Japanese journal of applied physics* 43.7S (2004), p. 4704.

10 E. Meinders, A. Mijiritskii, L. van Pieterson and M. Wuttig. *Optical Data Storage Phase-change Media and Recording*. Springer Dordrecht, 2006.

11 T. Ohta, K. Nishiuchi, K. Narumi, Y. Kitaoka, H. Ishibashi, N. Yamada and T. Kozaki. “Overview and the future of phase-change optical disk technology”. In: *Japanese Journal of Applied Physics* 39.2S (2000), p. 770.

12 N. Yamada, E. Ohno, K. Nishiuchi, N. Akahira and M. Takao. “Rapid-phase transitions of GeTe-Sb2Te3 pseudobinary amorphous thin films for an optical disk memory”. In: *Journal of Applied Physics* 69.5 (1991), pp. 2849–2856.

13 P. Noé, C. Vallée, F. Hippert, F. Fillot and J.-Y. Raty. “Phase-change materials for non-volatile memory devices: from technological challenges to materials science issues”. In: *Semiconductor Science and Technology* 33.1 (2017), p. 013002.

14 I. V. Karpov and S. A. Kostylev. “SET to RESET programming in phase change memories”. In: *IEEE electron device letters* 27.10 (2006), pp. 808–810.

15 G. W. B. et al. “Phase change memory technology”. In: *Journal of Vacuum Science & Technology B* 28 (2010), pp. 223–262.

16 S. Rajarajan, M. Prabhu and S. Karthikeyan. “A study on the challenges and prospects of pcm based main memory architectures”. In: *Middle-East Journal of Scientific Research* 18.6 (2013), pp. 788–795.

17 P. Fantini. “Phase change memory applications: the history, the present and the future”. In: *Journal of Physics D: Applied Physics* 53.28 (2020), p. 283002.

18 W. Wang, L. Shi, R. Zhao, K. Lim, H. Lee, T. Chong and Y. Wu. “Fast phase transitions induced by picosecond electrical pulses on phase change memory cells”. In: *Applied Physics Letters* 93.4 (2008).

19 Y. Qi, N. Chen, T. Vasileiadis, D. Zahn, H. Seiler, X. Li and R. Ernstorfer. “Photoinduced Ultrafast Transition of the Local Correlated Structure in Chalcogenide Phase-Change Materials”. In: *Physical Review Letters* 129 (2022), p. 135701.

20 L. Waldecker, T. A. Miller, M. Rudé, R. Bertoni, J. Osmond, V. Pruneri, R. E. Simpson, R. Ernstorfer and S. Wall. "Time-domain separation of optical properties from structural transitions in resonantly bonded materials". In: *Nature materials* 14.10 (2015), pp. 991–995.

21 E. Matsubara, S. Okada, T. Ichitsubo, T. Kawaguchi, A. Hirata, P. Guan, K. Tokuda, K. Tanimura, T. Matsunaga, M. Chen et al. "Initial atomic motion immediately following femtosecond-laser excitation in phase-change materials". In: *Physical review letters* 117.13 (2016), p. 135501.

22 P. Fons, H. Osawa, A. Kolobov, T. Fukaya, M. Suzuki, T. Uruga, N. Kawamura, H. Tanida and J. Tominaga. "Photoassisted amorphization of the phase-change memory alloy Ge 2 Sb 2 Te 5". In: *Physical Review B—Condensed Matter and Materials Physics* 82.4 (2010), p. 041203.

23 M. Jaskolski, Z. Dauter and A. Wlodawer. "A brief history of macromolecular crystallography, illustrated by a family tree and its N obel fruits". In: *The FEBS journal* 281.18 (2014), pp. 3985–4009.

24 J. C. Brooks-Bartlett and E. F. Garman. "The nobel science: One hundred years of crystallography". In: *Interdisciplinary Science Reviews* 40.3 (2015), pp. 244–264.

25 D. H. Bilderback, P. Elleaume and E. Weckert. "Review of third and next generation synchrotron light sources". In: *Journal of Physics B: Atomic, molecular and optical physics* 38.9 (2005), S773.

26 P. F. Tavares, S. C. Leemann, M. Sjöström and Å. Andersson. "The MAX IV storage ring project". In: *Synchrotron Radiation* 21.5 (2014), pp. 862–877.

27 M. Fuchs, R. Weingartner, A. Popp, Z. Major, S. Becker, J. Osterhoff, I. Cortrie, B. Zeitler, R. Hörlein, G. D. Tsakiris et al. "Laser-driven soft-X-ray undulator source". In: *Nature physics* 5.11 (2009), pp. 826–829.

28 H. Enquist, A. Jurgilaitis, A. Jarnac, Å. Bengtsson, M. Burza, F. Curbis, C. Disch, J. C. Ekström, M. Harb, L. Isaksson et al. "FemtoMAX–an X-ray beamline for structural dynamics at the short-pulse facility of MAX IV". In: *Synchrotron Radiation* 25.2 (2018), pp. 570–579.

29 D. Kroon, E. Nilsson, B. Ahn, M. Bertelli, R. Calarco, I. Clementsson, S. De Simone, J. Ekström, A. Jurgilaitis, M. Longo et al. "A cross-correlator-based timing tool for FemtoMAX". In: *Synchrotron Radiation* 32.4 (2025).

30 M. Smyth and J. Martin. “x Ray crystallography”. In: *Molecular Pathology* 53.1 (2000), p. 8.

31 E. Ameh. “A review of basic crystallography and x-ray diffraction applications”. In: *The international journal of advanced manufacturing technology* 105.7 (2019), pp. 3289–3302.

32 W. H. Miller. *A treatise on crystallography*. For J. & JJ Deighton, 1839.

33 P. P. Ewald. *Kristalle und Röntgenstrahlen*. Berlin: Springer, 1921.

34 W. L. Bragg. *The Crystalline State: The determination of crystal structures, by H. Lipson and W. Cochran*. Vol. 3. Cornell University Press, 1876.

35 W. H. Miller. “On the structure of crystals”. In: *Cambridge Philosophical Transactions* 6 (1839), pp. 397–460.

36 N. W. Ashcroft and N. D. Mermin. *Solid State Physics*. Holt-Saunders, 1976.

37 R. E. Peierls. “Quantum theory of solids”. In: Oxford University Press, 1955.

38 H. Beister, K. Strössner and K. Syassen. “Rhombohedral to simple-cubic phase transition in arsenic under pressure”. In: *Physical Review B* 41.9 (1990), p. 5535.

39 L. P. Bouckaert, R. Smoluchowski and E. Wigner. “Theory of Brillouin Zones and Symmetry Properties of Wave Functions in Crystals”. In: *Physical Review* 50.1 (1936), pp. 58–67.

40 T. Matsunaga, N. Yamada and Y. Kubota. “Structures of stable and metastable $Ge_2Sb_2Te_5$, an intermetallic compound in GeTe–Sb_2Te_3 pseudobinary systems”. In: *Acta Crystallographica Section B: Structural Science* 60.6 (2004), pp. 685–691.

41 M. Xu, Y. Cheng, H. Sheng and E. Ma. “”Nature of atomic bonding and atomic structure in the phase-change Ge2Sb2Te5 glass””. In: *Physical review letters* 103.19 (2009), p. 195502.

42 S. R. Ovshinsky. “Reversible electrical switching phenomena in disordered structures”. In: *Physical Review Letters* 21.20 (1968), pp. 1450–1453.

43 G. Pagare and et al. “Recent advances in doped $Ge_2Sb_2Te_5$ thin film-based phase-change memories”. In: *Materials Advances* (2023). Advance Article.

44 M. Wuttig and N. Yamada. “Phase-change materials for rewriteable data storage”. In: *Nature Materials* 6.11 (2007), pp. 824–832.

45 N. Yamada and T. Matsunaga. “Structure of laser-crystallized Ge2Sb2+xTe5 sputtered thin films for use in optical memory”. In: *Journal of Applied Physics* 88.10 (2000), pp. 7020–7028.

46 I. Satoh, S. Ohara, N. Akahira and M. Takenaga. “Key technology for high density rewritable DVD (DVD-RAM)”. In: *IEEE Transactions on Magnetics* 34.2 Pt.1 (1998), pp. 331–337.

47 A. V. Kolobov, P. Fons, A. I. Frenkel, A. L. Ankudinov and J. Tominaga. “Understanding the phase-change mechanism of rewritable optical media”. In: *Nature Materials* 3.9 (2004), pp. 703–708.

48 C. J. Foot. *Atomic Physics*. Oxford University Press, 2005.

49 B. E. A. Saleh and M. C. Teich. *Fundamentals of Photonics*. 2nd. Wiley-Interscience, 2007.

50 B. E. Warren. *X-ray Diffraction*. Originally published by Addison-Wesley, 1969. New York, Chapter 1: Dover Publications, 1990, pp. 1–5.

51 M. Laue, W. Friedrich and P. Knipping. “Interferenz-Erscheinungen bei Röntgenstrahlen”. In: *Annalen der Physik* 346.10 (1912), pp. 971–988.

52 P. P. Ewald. “Zur Begründung der Kristalloptik”. In: *Annalen der Physik* 345.6 (1913), pp. 253–287.

53 B. Dawson. “A general structure factor formalism for interpreting accurate X-ray and neutron diffraction data”. In: *Proceedings of the Royal Society A* 298 (1967), pp. 255–263.

54 P. Coppens. “The structure factor”. In: *International Tables for Crystallography, Volume B: Reciprocal Space*. Ed. by U. Shmueli. International Union of Crystallography, 2010, pp. 159–160.

55 H. P. Klug and L. E. Alexander. *X-ray Diffraction Procedures: For Polycrystalline and Amorphous Materials*. 2nd ed. New York: Wiley-Interscience, 1974.

56 R. James. *The Optical Principles of the Diffraction of X-rays*. London: G. Bell and sons LTD, 1962.

57 T. R. Welberry. *Diffuse X-ray Scattering and Models of Disorder*. Oxford: Oxford University Press, 2004.

58 B. Warren and B. Averbach. “THE DIFFUSE” SCATTERING OF X-RAYS””. In: (1953).

59 A. Guinier. *X-ray Diffraction in Crystals, Imperfect Crystals, and Amorphous Bodies*. Reprint of Addison-Wesley edition, 1963. New York: Dover Publications, 1994.

60 K. Y. Lonsdale and H. Smith. "An experimental study of diffuse X-ray reflection by single crystals". In: *Proceedings of the Royal Society A* 179 (1941).

61 J. E. Eldridge and T. R. Lomer. "An experimental study of the diffuse X-ray scattering from sodium chloride". In: *Proceedings of the Physical Society* 91.2 (1967), pp. 325–329.

62 T. R. Welberry and T. Weber. "One hundred years of diffuse scattering". In: *Crystallography Reviews* 22.1 (2016), pp. 2–78.

63 C. Kittel. *Introduction to Solid State Physics*. 8th ed. Wiley, Chapter 4, 2005.

64 C. Kittel. *Introduction to Solid State Physics*. 8th ed. Wiley, Chapter 3, 2005.

65 I. Waller. "Zur Frage der Einwirkung der Wärmebewegung auf die Interferenz von Röntgenstrahlen". In: *Zeitschrift für Physik* 17 (1913).

66 P. Debye. "Interferenz von Röntgenstrahlen und Wärmebewegung". In: *Annalen der Physik* 348 (1913).

67 B. Warren. *X-ray Diffraction, Chapter 11*. New York: Dover Publications, INC., 1969.

68 C. Kittel. *Introduction to Solid State Physics*. 8th ed. Wiley, Chapter 8, 2005.

69 A. Stoneham. "Non-radiative transitions in semiconductors". In: *Reports on Progress in Physics* 44.12 (1981), p. 1251.

70 W. Knox, D. Chemla, G. Livescu, J. Cunningham and J. Henry. "Femtosecond carrier thermalization in dense Fermi seas". In: *Physical review letters* 61.11 (1988), p. 1290.

71 Y.-C. Wen, C.-Y. Chen, C.-H. Shen, S. Gwo and C.-K. Sun. "Ultrafast carrier thermalization in InN". In: *Applied physics letters* 89.23 (2006).

72 Z. Nie, R. Long, L. Sun, C.-C. Huang, J. Zhang, Q. Xiong, D. W. Hewak, Z. Shen, O. V. Prezhdo and Z.-H. Loh. "Ultrafast carrier thermalization and cooling dynamics in few-layer MoS2". In: *ACS nano* 8.10 (2014), pp. 10931–10940.

73 J. Shah. “Hot electrons and phonons under high intensity photoexcitation of semiconductors”. In: *Solid-State Electronics* 21.1 (1978), pp. 43–50.

74 D. K. Ferry. “Non-equilibrium longitudinal optical phonons and their lifetimes”. In: *Applied Physics Reviews* 8.2 (2021).

75 P. Klemens. “Anharmonic decay of optical phonons”. In: *Physical Review* 148.2 (1966), p. 845.

76 B. Ridley and R. Gupta. “Nonelectronic scattering of longitudinal-optical phonons in bulk polar semiconductors”. In: *Physical review B* 43.6 (1991), p. 4939.

77 F. Vallée and F. Bogani. “Coherent time-resolved investigation of LO-phonon dynamics in GaAs”. In: *Physical Review B* 43.14 (1991), p. 12049.

78 F. Stillinger and T. Weber. “Lindemann melting criterion and the Gaussian core model”. In: *Physical Review B* 22.8 (1980), p. 3790.

79 A. C. Lawson. “Physics of the Lindemann melting rule”. In: *Philosophical Magazine* 89.22-24 (2009), pp. 1757–1770.

80 F. A. Lindemann. “Ueber die berechnung molekularer eigenfrequenzen”. In: *Phys. Z* 11 (1910), pp. 609–612.

81 A. M. Lindenberg, J. Larsson, K. Sokolowski-Tinten, K. Gaffney, C. Blome, O. Synnergren, J. Sheppard, C. Caleman, A. MacPhee, D. Weinstein et al. “Atomic-scale visualization of inertial dynamics”. In: *Science* 308.5720 (2005), pp. 392–395.

82 X. Wang, J. C. Ekström, Å. U. J. Bengtsson, A. Jarnac, A. Jurgilaitis, V.-T. Pham, D. Kroon, H. Enquist and J. Larsson. “Role of Thermal Equilibrium Dynamics in Atomic Motion during Nonthermal Laser-Induced Melting”. In: *Phys. Rev. Lett.* 124 (10 2020), p. 105701.

83 C. Rose-Petruck, R. Jimenez, T. Guo, A. Cavalleri, C. W. Siders, F. Rksi, J. A. Squier, B. C. Walker, K. R. Wilson and C. P. Barty. “Picosecond–milliångström lattice dynamics measured by ultrafast X-ray diffraction”. In: *Nature* 398.6725 (1999), pp. 310–312.

84 A. Lindenberg, I. Kang, S. L. Johnson, T. Missalla, P. Heimann, Z. Chang, J. Larsson, P. Bucksbaum, H. Kapteyn, H. Padmore et al. “Time-resolved x-ray diffraction from coherent phonons during a laser-induced phase transition”. In: *Physical review letters* 84.1 (2000), p. 111.

85 C. W. Siders, A. Cavalleri, K. Sokolowski-Tinten, C. Toth, T. Guo, M. Kammler, M. H. v. Hoegen, K. R. Wilson, D. v. d. Linde and C. P. Barty. "Detection of nonthermal melting by ultrafast X-ray diffraction". In: *Science* 286.5443 (1999), pp. 1340–1342.

86 K. Gaffney, A. Lindenberg, J. Larsson, K. Sokolowski-Tinten, C. Blome, O. Synnergren, J. Sheppard, C. Caleman, A. MacPhee, D. Weinstein et al. "Observation of Structural Anisotropy and the Onset of Liquidlike Motion During the Nonthermal Melting of InSb". In: *Physical review letters* 95.12 (2005), p. 125701.

87 W. Lu, M. Nicoul, U. Shymanovich, A. Tarasevitch, M. Kammler, M. H. von Hoegen, D. von der Linde and K. Sokolowski-Tinten. "Transient reversal of a Peierls-transition: Extreme phonon softening in laser-excited Bismuth". In: *International Conference on Ultrafast Phenomena*. Optica Publishing Group. 2010, ME41.

88 M. Trigo, J. Chen, V. Vishwanath, Y.-M. Sheu, T. Graber, R. Henning and D. Reis. "Imaging nonequilibrium atomic vibrations with x-ray diffuse scattering". In: *Physical Review B—Condensed Matter and Materials Physics* 82.23 (2010), p. 235205.

89 M. Trigo, M. Fuchs, J. Chen, M. Jiang, M. Cammarata, S. Fahy, D. M. Fritz, K. Gaffney, S. Ghimire, A. Higginbotham et al. "Fourier-transform inelastic X-ray scattering from time-and momentum-dependent phonon–phonon correlations". In: *Nature Physics* 9.12 (2013), pp. 790–794.

90 A. Cavalleri, T. Dekorsy, H. H. Chong, J.-C. Kieffer and R. W. Schoenlein. "Evidence for a structurally-driven insulator-to-metal transition in VO 2: A view from the ultrafast timescale". In: *Physical Review B—Condensed Matter and Materials Physics* 70.16 (2004), p. 161102.

91 A. S. Johnson, D. Perez-Salinas, K. M. Siddiqui, S. Kim, S. Choi, K. Volckaert, P. E. Majchrzak, S. Ulstrup, N. Agarwal, K. Hallman et al. "Ultrafast X-ray imaging of the light-induced phase transition in VO2". In: *Nature Physics* 19.2 (2023), pp. 215–220.

92 P. Zalden, F. Quirin, M. Schumacher, J. Siegel, S. Wei, A. Koc, M. Nicoul, M. Trigo, P. Andreasson, H. Enquist et al. "Femtosecond x-ray diffraction reveals a liquid–liquid phase transition in phase-change materials". In: *Science* 364.6445 (2019), pp. 1062–1067.

93 H. Seiler, D. Zahn, V. C. Taylor, M. I. Bodnarchuk, Y. W. Windsor, M. V. Kovalenko and R. Ernstorfer. “Direct observation of ultrafast lattice distortions during exciton–polaron formation in lead halide perovskite nanocrystals”. In: *ACS nano* 17.3 (2023), pp. 1979–1988.

94 H. Ueda, R. Mankowsky, E. Paris, M. Sander, Y. Deng, B. Liu, L. Leroy, A. Nag, E. Skoropata, C. Wang et al. “Non-equilibrium dynamics of spin-lattice coupling”. In: *Nature Communications* 14.1 (2023), p. 7778.

95 Y. S. Chu, C. Liu, D. C. Mancini, F. de Carlo, A. T. Macrander, B. Lai and D. Shu. “Performance of a double-multilayer monochromator at Beamline 2-BM at the Advanced Photon Source”. In: *Review of Scientific Instruments* 73.3 (2002), pp. 1485–1487.

96 P. K. Wong et al. “A high-performance double-crystal monochromator soft X-ray beamline”. In: *Journal of Synchrotron Radiation* 5.3 (1998). Describes a Cam-type DCM design with details on thermal load, crystal movement, and beam stability, pp. 204–210.

97 S. Sen, T. G. Edwards, J.-Y. Cho and Y.-C. Joo. “Te-Centric View of the Phase Change Mechanism in Ge-Sb-Te Alloys”. In: *Phys. Rev. Lett.* 108 (19 2012), p. 195506.

98 A. Kolobov, P. Fons, J. Tominaga and M. Hase. “Excitation-assisted disordering of GeTe and related solids with resonant bonding”. In: *The Journal of Physical Chemistry C* 118.19 (2014), pp. 10248–10253.

99 X.-B. Li, X. Liu, X. Liu, D. Han, Z. Zhang, X. Han, H.-B. Sun and S. Zhang. “Role of electronic excitation in the amorphization of Ge-Sb-Te alloys”. In: *Physical review letters* 107.1 (2011), p. 015501.

100 K. Shportko, S. Kremers, M. Woda, D. Lencer, J. Robertson and M. Wuttig. “Resonant bonding in crystalline phase-change materials”. In: *Nature materials* 7.8 (2008), pp. 653–658.